

DRAFT v0.2 (29 AUGUST 2024)

Introduction to Dark Matter and Dark Sector Models and Searches

Yi-Ming Zhong^a

^a City University of Hong Kong, 83 Tat Chee Avenue, Kowloon, Hong Kong SAR, China

E-mail: yiming.zhong@cityu.edu.hk

ABSTRACT: Lecture notes for the 28th International Summer Institute on Phenomenology of Elementary Particle Physics and Cosmology (SI2024) at Linyi, Shangdong, China.

Contents

1	Introduction	1
2	First lecture	2
2.1	Evidence for dark matter	2
2.2	Basic properties of dark matter	2
2.3	Dark matter with dark sector mediators	6
2.4	Complementarity of different probes	7
2.5	The wall: N_{eff} constraints	12
3	Second lecture	18
3.1	Small-scale power spectrum: probing dark matter in the early universe	19
3.1.1	The power spectrum of CDM	21
3.1.2	The power spectrum of dark matter beyond CDM	22
3.1.3	Observations	26
3.2	Inside dark matter halos: self-interacting dark matter	27
3.2.1	A qualitative understanding	28
3.2.2	Astrophysical probes and the velocity-dependent SIDM	29
A	Units	31
B	Cosmology for students in a hurry	32
B.1	Background	32
B.2	Thermodynamics in the early universe	33
B.3	Dark matter thermal freeze-out and the WIMP miracle	34

1 Introduction

Two statements summarize our understanding of dark matter today: (1) dark matter exists, and (2) its nature remains elusive. There is a wealth of textbooks, reviews, community reports, lecture notes, and video records on the subject of dark matter. Notable recent contributions include the review by [1], the textbooks by [2, 3], the TASI lectures by [4–6], which I heavily relied on in making this lecture notes. Given the vast scope of dark matter modeling and detection, it is impossible to cover all aspects comprehensively in these lectures. Therefore, we will focus on an emerging paradigm I have been working on, where dark matter is considered a part of the dark sectors. In this framework, additional particles in the dark sector serve as mediators for interactions between dark matter and ordinary matter, and for interactions among dark matter themselves. The content is arranged as follows: In Lecture I, we will overview dark matter physics and explore the complementarity

of various probes of dark matter/dark sector from the intensity frontier experiments. Lecture II will focus on the observational signatures of dark matter physics at the small-scale structures.

Before concluding, I would like to share my favorite quote:

“It is difficult but interesting to master ten percent of any field. The path from ten to ninety percent is pure pleasure and genuine creativity. To go through the next nine percent is infinitely difficult, and far from everyone’s ability. The last percent is hopeless. It is more reasonable to switch to a new problem before it is too late.”

— Yakov Zel’dovich

2 First lecture

2.1 Evidence for dark matter

Over the past nine decades, since Zwicky first proposed dark matter to explain the unexpected concentration of galaxies in the Coma cluster [7], evidence supporting its existence has accumulated across multiple cosmic scales. Dark matter has become an indispensable ingredient of the standard cosmology model, Λ CDM, where Λ represents the cosmological constant while CDM stands for the “cold dark matter.” Dark matter has successfully explained various astronomical and cosmological observations, including the behavior of galaxy clusters, galaxy rotation curves, bullet cluster crossing, cosmic shears, the formation of large-scale structure (LSS), and the patterns in the cosmic microwave background (CMB). See e.g. [8, 9] for a review. Fig. 1 presents a timeline of significant events in the development of dark matter physics. In this timeline, events highlighted in color represent primary observational evidence supporting the existence of dark matter. The black text shows important proposed dark matter candidates, related phenomena, or key methodologies used in dark matter research.

2.2 Basic properties of dark matter

Nevertheless, the nature of dark matter remains elusive. The statement does not mean we do not know any properties of dark matter. We have a good understanding of dark matter’s behavior on large cosmological scales. To agree with observations from the CMB, Big Bang nucleosynthesis (BBN), and LSS, dark matter must be:

- Cold: dark matter is non-relativistic ($v \ll c$) during the gravitational collapse.
- Non-baryonic
- Stable
- The abundance of dark matter today is $\Omega_\chi h^2 = 0.1200 \pm 0.001$ where $h = 0.674 \pm 0.005$ is the reduced Hubble constant from Planck 2018 [10]. The abundance corresponds to a background dark matter density of $\rho_\chi = 1.3 \text{ keV cm}^{-3} \simeq 10^{-11} \text{ eV}^4$.¹

¹Here and below, we use the natural unit $\hbar = c = k_B = 1$. See Appendix A for more details.

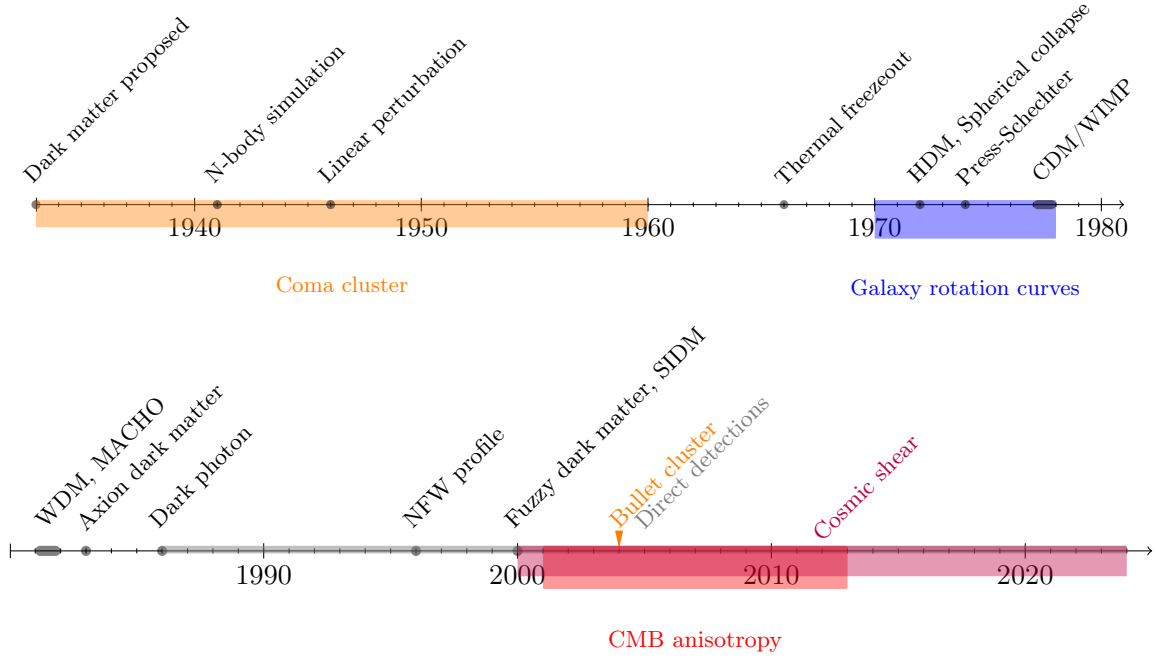


Figure 1. A brief history of dark matter and related theories and methodologies. Source: [1, 8, 9]. Acronym: CDM: cold dark matter; HDM: hot dark matter; WDM: warm dark matter; SIDM: self-interacting dark matter; WIMP: weakly-interacting massive particle; MACHO: massive compact halo object.

Dark matter is about five times greater than that of the baryonic matter. While this factor of five may seem significant, it is relatively small compared to the ratio of dark matter abundance to the photon abundance today ($\Omega_\gamma h^2 = 2 \times 10^{-5}$), which is about 5,000 times. The closeness in the abundance between dark matter and baryons leads to the ideas such as asymmetric dark matter.

- Adiabatic: Dark matter has the same primordial density fluctuations as baryons, photons, and neutrinos on the cosmic scale. The constraint from CMB anisotropy on the departure from the adiabatic fluctuations is about $\mathcal{O}(10^{-2})$.

The adiabatic property is usually used to constrain multi-field inflation models. Some recent attempts tried to use the properties to constrain dark matter production via freeze-in [11], and later studies found the observational constraints are not strong at all [12–15].

Small-scale observations also provide values on dark matter’s local density and constrain dark matter’s “particle” mass, whether as an individual particle or a single composite object:

- The local dark matter density is $\rho_\chi = 0.4 \text{ GeV cm}^{-3} \simeq (0.04 \text{ eV})^4$ [16].
- Dark matter cannot be too light, $m \gtrsim 10^{-22} \text{ eV}$, as its de Broglie wavelength would then exceed the virial radius of a dwarf galaxy. Otherwise, the bulk of the dwarf halo

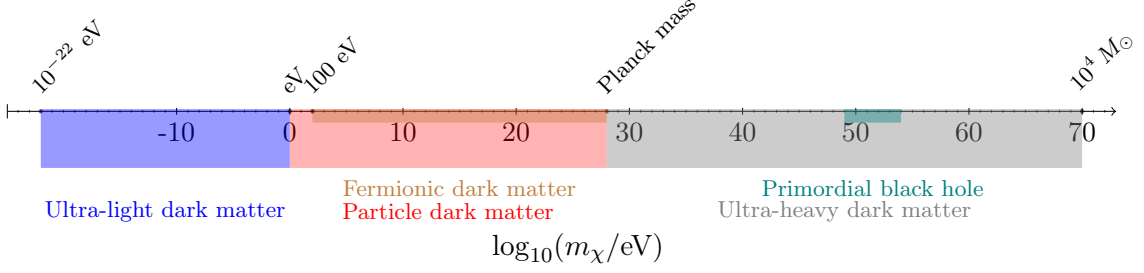


Figure 2. Important mass scales for dark matter candidates between 10^{-22} eV and $10^4 M_\odot$. We split them into ultra-light dark matter ($\lesssim 1 \text{ eV}$), particle dark matter ($1 \text{ eV} - m_{\text{pl}}$), ultra-heavy dark matter ($\gtrsim m_{\text{pl}}$). We also show the mass range for fermionic particle dark matter and the primordial black hole that can consist 100% of dark matter.

will reside in the solitonic region with an ultra-high density that is in tension with observations [17].

- Dark matter cannot be too heavy, $m \lesssim 10^4 M_\odot$, as there should be a sufficient number of particles to populate a dwarf galaxy such that its density distribution and gravitational field are mostly smooth and do not show granularity.

The mass of dark matter “particles” spans over 90 orders of magnitude ($1 M_\odot \simeq 10^{66} \text{ eV} \simeq 2 \times 10^{33} \text{ g}$). However, it is still finite. Fig. 2 shows the landscape of dark matter mass. Note that there are a few important mass scales on the vast range:

- $m_\chi = m_{\text{pl}} \simeq 10^{28} \text{ eV} \simeq 22 \mu\text{g}$, above which a single dark matter particle’s Compton wavelength will be within its Schwarzschild radius

$$m_\chi \gtrsim m_{\text{pl}} \Rightarrow \frac{1}{m_\chi} \lesssim Gm_\chi = \frac{m_\chi}{m_{\text{pl}}^2}. \quad (2.1)$$

Therefore, for dark matter “particle” with $m_\chi > m_{\text{pl}}$, what we mean by “particle” is not a particle but a single composite object such as primordial black holes or a bag of dark matter particles. We call those candidates ultra-heavy dark matter.

- $m_\chi = 100 \text{ eV}$. If dark matter is fermionic, a halo can be considered as a self-gravitating degenerate Fermi gas system. For such a halo to exist, the Fermi velocity v_F , which is given by

$$v_F = \sqrt{\frac{2E_F}{m_\chi}} = \left(\frac{6\pi^2 \rho_\chi}{g_\chi m_\chi^4} \right)^{1/3} \quad (2.2)$$

where $E_F = \frac{1}{2m_\chi} \left(\frac{6\pi^2 \rho_\chi}{g_\chi m_\chi} \right)^{2/3}$ is the Fermi energy and g_χ is the number of spin and flavor states, should not exceed the escape velocity of the halo. Assuming a halo has a uniform density, the condition yields

$$v_F \leq \sqrt{\frac{2GM_h}{r_h}} \Rightarrow m_\chi \gtrsim g_\chi^{-1/4} G^{-3/8} M_h^{-1/8} r_h^{-3/8}, \quad (2.3)$$

	Neutrinos	Dark Matter
Number of species	Three flavors	?
Mass	$0 - 0.8$ eV	$10^{-22} - 10^{70}$ eV
(Sum of masses)	$0.059 - 0.113$ eV	??
Spin	$1/2$?
Electric charge	0	$\lesssim 10^{-10} - 10^{-1}$
Self-interaction	Electroweak & ?	Gravity & ?
Int. w/ other particles	Electroweak & ?	Gravity & ?
Lifetime	$\gtrsim 6 \times 10^{15}$ s	$\gtrsim 4.4 \times 10^{17}$ s
Decay channel	?	?
Cosmic production	Decoupled from SM plasma at $T \sim 1$ MeV	?
Other prod. channel	Stars, cosmic rays, reactors, accelerators ...	?
Abundance today	$(1.4 - 2.7) \times 10^{-3}$	0.264
% of the total mass	$(0.4 - 0.9)\%$	84%
ρ_{bkg}	$(6.7 - 13)$ eV cm $^{-3}$	1.3 keV cm $^{-3}$
n_{bkg}	$3 \times 2 \times 56$ cm $^{-3}$	$10^{-67} - 10^{25}$ cm $^{-3}$
Clustering	No	Yes
ρ_{local}	$\sim \rho_{\text{bkg}}$	0.4 GeV cm $^{-3}$
n_{local}	$\sim n_{\text{bkg}}$	$10^{-62} - 10^{30}$ cm $^{-3}$
Momentum dist.	Fermi-Dirac	?

Table 1. Properties of neutrinos and dark matter [1, 19, 20]. The neutrino column’s lower section lists the properties of cosmic relic neutrinos. We cite the limits from DESI baryon acoustic oscillation (BAO) + CMB for the total neutrino mass, assuming the neutrino masses follow the normal hierarchy [21]. The cosmic neutrino abundance and its percentage of the total mass are calculated accordingly with cosmological parameters from [10].

where M_h and r_h are the halo mass and radius, respectively. Eq. (2.3) indicates that stronger constraints can be obtained from a smaller halo. Ref. [18] analyzes Leo II, a dwarf galaxy, and imposes constraints of $m_\chi \geq 0.13$ keV for fermionic dark matter with $g_\chi = 2$.

- $m_\chi = 1$ eV, below which particles’ de Broglie wavelength overlap.

$$\frac{1}{m_\chi v_\chi} \geq \left(\frac{\rho_\chi}{m_\chi} \right)^{-1/3} \Rightarrow m_\chi \leq \rho_\chi^{-1/4} v_\chi^{-3/4} \sim \mathcal{O}(\text{eV}). \quad (2.4)$$

Sub-eV dark matter particles should be thought of as wave-like (like classical electromagnetic field) rather than particle-like. Those candidates are known as ultra-light dark matter.

What we mean by “the nature of dark matter remains elusive” is that we do not understand the properties of dark matter as comprehensive as other Standard Model particles. Tab. 1 compares dark matter to neutrinos, the least understood corner of the ordinary matter. Unlike neutrinos, we still lack an understanding of dark matter’s spin, the number

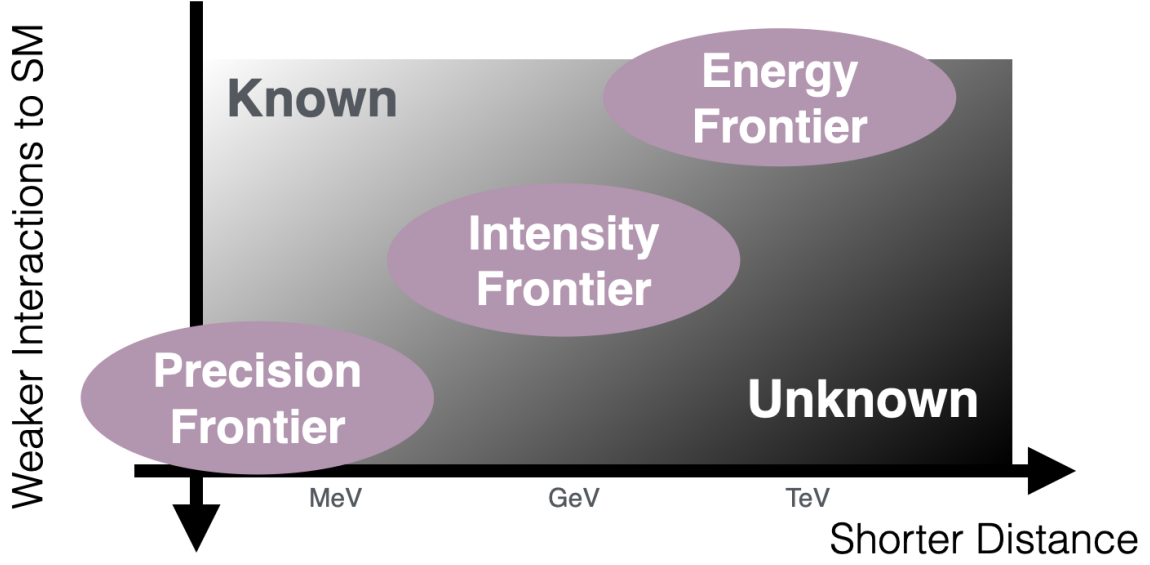


Figure 3. Frontiers in particle physics

of species, and production mechanisms. Constraints on the dark matter mass and its local number density are much looser than those of neutrinos. We are also unsure if dark matter can be produced on Earth or far-away stars.

The elusive nature of dark matter is both a challenge and an opportunity. It simulates theorists to propose new models and enables experimentalists to invent new search schemes. Meanwhile, despite the limited understanding of dark matter, people have been using the distribution of dark matter to probe what happens in the early universe and other fundamental physics.

2.3 Dark matter with dark sector mediators

The Standard Model includes numerous bosons and fermions with intricate interactions. A similar situation might occur with dark matter, potentially existing within dark sectors composed of feebly interacting particles, such as dark photons and dark Higgs. The concept of dark sectors can be traced back to the hidden sectors involved in supersymmetry breaking (see review [22]) and the hidden valleys [23]. This idea gained popularity when [24] employed the Sommerfeld-enhanced dark matter annihilation, a phenomenon involving a light dark mediator, to explain the PAMELA positron excess [25]. Over the past decade, light dark sector particles have appeared crucial in addressing numerous other puzzles in particle physics, such as the muon $g - 2$, neutron lifetime [26], proton charge radius [27], and the ATOMKI anomaly [28]. Among the notable examples of the dark sector particles are the “*fabulous five*”:²

- Dark photon, A' ,
- Dark Higgs, S ,

²Source: Prof. Lian-Tao Wang.

- Axion-like particle, a ,
- Sterile neutrino, N ,
- Millicharged particle³.

Their interactions with the Standard Model sector are through various “portals”:

- Vector portal with kinetic mixing: $\epsilon F_{\mu\nu} F'^{\mu\nu}$
- Vector portal with $U(1)_{B-L}$: $A'_\mu J_{B-L}^\mu$
- Higgs portal: $H^\dagger H(\lambda S^2 + AS)$
- Neutrino portal: LHN
- Axion portal: $\frac{1}{f} \partial_\mu a J_A^\mu$
- ...

The growing interest in dark sector particles and portal interactions signifies a paradigm shift in the particle physics community. This new perspective acknowledges that new physics can occur at both higher and lower energies (see Fig. 3). Consequently, we should fully leverage available facilities and technologies to explore new light physics. This shift is evident in the blooming of intensity frontier experiments, such as flavor factories, fixed-target experiments, muon experiments, and neutrino experiments, as well as precision frontier experiments, including the muon $g - 2$, electron’s electric dipole moment, and the fifth force search.

2.4 Complementarity of different probes

Let us consider a concrete example to illustrate the complementarity of different probes to search for a light dark sector. We consider the dark matter candidate a Dirac fermion χ , with the *real* scalar mediator S coupling only to Standard Model leptons.

$$\mathcal{L} \supset -g_\chi S \bar{\chi} \chi - \sum_{\ell=e,\mu,\tau} g_\ell S \bar{\ell} \ell. \quad (2.5)$$

The couplings of S to leptons can be understood as originating from the effective gauge-invariant dimension-5 operators:

$$\frac{c_i}{\Lambda} S \bar{L}_i H E_i. \quad (2.6)$$

Here, Λ is the associated scale of new physics, and c_i is a Wilson coefficient for flavor i . We will assume that the couplings are diagonal in the mass basis. While the relative sizes of the Wilson coefficients c_i (and hence the effective couplings g_i) are undetermined *a priori*, a natural expectation might be that they are proportional to the corresponding Yukawa

³The millicharged particle can be considered as a new particle coupled to a massless dark photon.

coupling y_i , so that the effective g_i are proportional to the corresponding lepton masses after electroweak symmetry breaking, i.e.,

$$g_e : g_\mu : g_\tau = m_e : m_\mu : m_\tau. \quad (2.7)$$

This is the case in the framework of Minimal Flavor Violation. For Wilson coefficients $c_\ell \sim \mathcal{O}(1) \times y_\ell$ in Eq. (2.6), new physics scales $\Lambda \gtrsim 1$ TeV correspond to muon couplings $g_\mu \lesssim \mathcal{O}(10^{-4} - 10^{-3})$.

The S -lepton couplings in (2.5) also introduce effective scalar couplings to a pair of vector bosons (SVV) at one-loop. For a light scalar with mass below the electroweak scale, the most relevant SVV coupling is the scalar-diphoton coupling ($S\gamma\gamma$). This interaction is important when the decays of $S \rightarrow \ell^+\ell^-$ are kinematically forbidden. The interactions can be described by an effective Lagrangian,

$$\mathcal{L} \supset -\frac{1}{4}g_{\gamma\gamma}SF_{\mu\nu}F^{\mu\nu}, \quad g_{\gamma\gamma} = \frac{\alpha}{2\pi} \left| \sum_{\ell=e,\mu,\tau} \frac{g_\ell}{m_\ell} F_{1/2} \left(\frac{4m_\ell^2}{p_S^2}, \frac{q^2}{4m_\ell^2} \right) \right|, \quad (2.8)$$

where α is the electromagnetic fine structure constant and $F_{1/2}$ is a form factor that depends on the four-momentum-square of one of the photons (q^2) and the scalar S (p_S^2). See [29] for more details.

Turn our attention to dark matter. There are three distinct possibilities for the relative sizes of m_χ and m_S , each carrying different phenomenological consequences:

- $m_\chi < m_S/2$: In this case, if $g_\chi \gtrsim g_{e,\mu,\tau}$, the mediator S will primarily decay invisibly to $\chi\bar{\chi}$. The thermal freeze-out relic abundance of dark matter is driven by s -channel annihilation into leptons, $\bar{\chi}\chi \rightarrow \bar{\ell}\ell$ (or $\gamma\gamma$) in the early Universe. The annihilation rate is roughly given by

$$\langle\sigma v\rangle = 2\pi \frac{\alpha_D \alpha_\ell}{m_\chi} \frac{(m_\chi^2 - m_\ell^2)^{3/2}}{(m_S^2 - 4m_\chi^2)^2} \langle v_{\text{rel}}^2 \rangle, \quad (2.9)$$

where $\alpha_{D(\ell)} \equiv g_{D(\ell)}^2/(4\pi)$ and $\langle v_{\text{rel}}^2 \rangle$ is the thermal average of the relative dark matter velocity squared, reflecting the fact that annihilation is a p -wave process in this scenario. To get p -wave annihilation motivates us to choose a scalar mediator with a Dirac fermion dark matter for the light dark sector.

Why do we prefer p -wave annihilation? Observations of the CMB constrain the amount of energy injected into the Intergalactic Medium (IGM) through dark matter annihilation at late times, which can distort the CMB. However, this is only an issue if the dark matter annihilation cross-section is s -wave [30–32]. A p -wave annihilation cross-section can effectively evade these CMB constraints.

- $m_S/2 \lesssim m_\chi \lesssim m_S$: In this case, s -channel annihilation into leptons again sets the relic abundance of χ , providing a thermal relic target. However, $S \rightarrow \chi\bar{\chi}$ decays are kinematically forbidden, so S will decay visibly.

- $m_S < m_\chi$: In this case, S again decays visibly. However, annihilation in the early Universe will primarily proceed through secluded annihilation, $\bar{\chi}\chi \rightarrow SS$. The cross-section for this process only depends on the dark sector coupling g_χ , so there is no well-defined thermal relic target for terrestrial experiments.

Here we focus on the first scenario with $m_\chi < m_S/2$, since it provides concrete thermal targets and is generally difficult to test, given the invisible decays of S . Fig. 4 from Ref. [29] presents various constraints on the dark sector model assuming $m_\chi = m_S/3$. It is a busy plot. The various shaded regions and lines indicate existing and future probes of the model, respectively, forming a tight complementarity for the parameter space. We will summarize the major constraints as the “floor”, the “ceiling”, the “fence” and “walls” at the lighter end of the dark scalar/dark matter mass.

- **The floor: Relic abundance.** Regions below the red curves are excluded due to an overabundance of dark matter for the mass ratio $m_S/m_\chi = 3$. This can be understood as smaller couplings being more easily caught up by the universe’s expansion, ending the freeze-out at a higher temperature. For a rough estimate, set

$$\langle\sigma v\rangle \sim 2\pi\alpha_D\alpha_\mu\frac{m_\chi^2}{m_S^2} \sim 3 \times 10^{-26} \text{ cm}^3/\text{s} = \frac{1}{(20 \text{ TeV})^2} \quad (2.10)$$

yielding $g_\mu \sim 10^{-3}$ at $m_S = 1 \text{ GeV}$ ($m_S/m_\chi = 3$, $\alpha_D = 1/4\pi$). The benchmark value $\langle\sigma v\rangle$ is derived from the observed dark matter relic abundance under the dark matter freeze-out scenario. See Appendix B.3 for more details. The kinks in the red curves around $m_S = 2m_\mu$ and $m_S = 2m_\tau$ occur when a new annihilation channel becomes kinematically accessible as indicated by Eq. (2.9), which allow a drop in the couplings.

Note that the constraints from the relic abundance could change dramatically by the resonant enhancement, which occurs when $m_S \approx 2m_\chi$. In such a limit, $\langle\sigma v\rangle$ can be greatly enhanced, and the overabundance floor will move downward considerably.

- **The ceiling: Searches in collider and accelerator, rare decays.** The best way to search for light dark sector particles is through intensity frontier experiments, including fixed target experiments, rare decays, flavor factories, high-luminosity collider experiments, and neutrino experiments. Because we assume dark scalars predominantly couple to dark matter rather than Standard Model particles (which are severely constrained), the signals we look for include missing momentum/energy, partially invisible decays, or mono-photon signals.

Take NA64- μ , the fixed-target experiment with a muon beam at CERN, as an example. The setup is shown in the left panel of Fig. 5. It shoots a 100 GeV muon beam at a lead target and looks for events with large missing momentum using the trackers and hadronic calorimeter behind the target. If the dark scalar is produced through the bremsstrahlung process $\mu N \rightarrow \mu NS(\bar{\chi}\chi)$ (right panel of Fig. 5), it will appear as

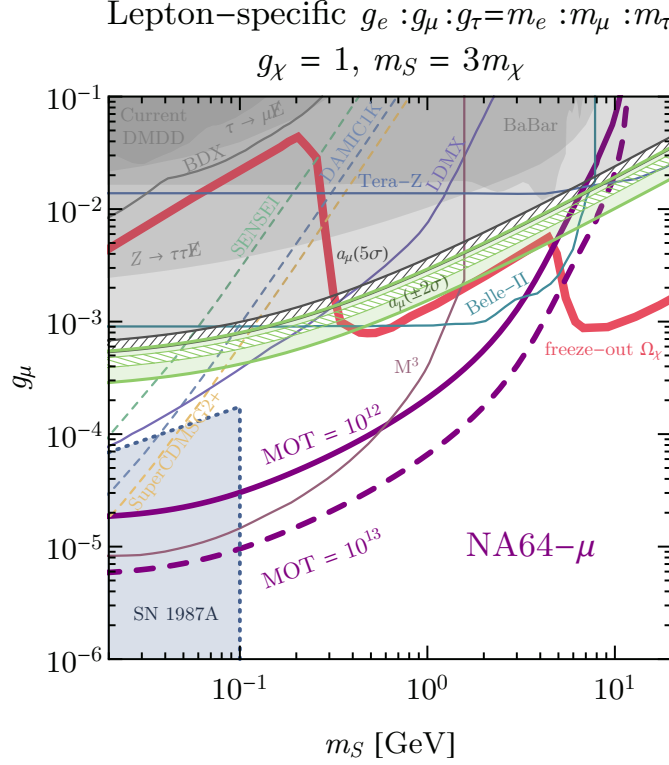


Figure 4. Current (shaded regions) and projected (lines) constraints for the dark matter-lepton-specific mediator model in the $g_\mu - m_S$ parameter space. We assume $m_\chi = m_S/3$ and $g_\chi = 1$. All the constraints are at 95% CL. The red curve indicates the parameters required to reach the correct thermal freeze-out dark matter abundance. The green and gray regions represent the 2σ -favored and 5σ -excluded regions based on current a_μ measurements. The blue region represents approximate exclusions from the cooling of SN 1987A. The shaded gray regions are limits from light dark matter direct detection experiments, XENON 10/100, DarkSide-50, and CDMS HVeV (collectively denoted as "current DMDD"), exotic Z and τ decays, and mono- γ searches at BaBar [33]. Colored lines are the sensitivity projections for NA64- μ , M^3 [34], LDMX [35], BDX [36], mono-photon searches at Belle-II [33], and Tera-Z [37], and expected DMDD limits from SENSEI, DAMIC-1K, and SuperCDMS-G2+.

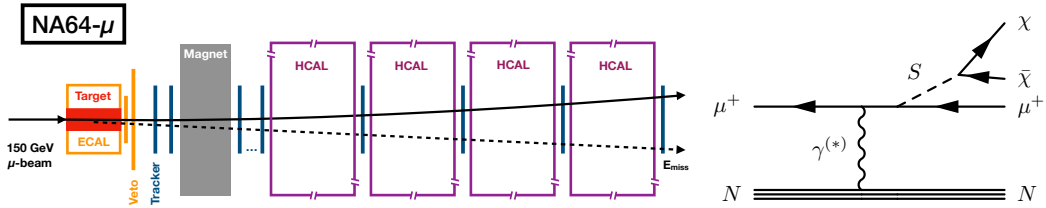


Figure 5. Left: The detector segment of the proposed NA64- μ experimental setup. Right: A diagram that leads to a muon missing momentum event.

a missing momentum event. The number of missing momentum events, N_χ , can be estimated as

$$N_\chi \sim N_\mu \times (n_{\text{atom}} y \sigma_{\mu N \rightarrow \mu N S}) \quad (2.11)$$

where $N_\mu = 10^{13}$ is the total number of muons on target, $n_{\text{atom}} = 10^{22} \text{ cm}^{-3}$ is the atomic number density of a lead target. y is the muon beam penetration length, which we approximate it with the target length of 20 cm. The bremsstrahlung process $\mu N \rightarrow \mu NS(\bar{\chi}\chi)$ can be treated using the improved Weizsacker-Williams approximation, which treats the virtual photon between the muon and lead atom as a real photon given the smallness of the transfer momentum $q^2 \approx 0$. Under the approximation, the cross section for $m_S \ll m_\mu$ can be estimated as

$$\sigma_{\mu N \rightarrow \mu NS} \sim \underbrace{\frac{\pi \alpha_\mu \alpha}{m_\mu^2}}_{\sigma_{\gamma N \rightarrow NS}} \times \underbrace{\alpha}_{\gamma NN \text{ vertex}} \times Z^2, \quad (2.12)$$

where Z is the atomic number of the lead. The enhancement of Z^2 comes from the elastic scattering between the muon and all protons in the atom. Requiring at least three N_χ events to be observed leads to $g_\mu \sim \mathcal{O}(10^{-5})$. A more careful analysis can be found in [29], which yields $g_\chi \sim 10^{-5}$. As the scalar mass becomes more massive, it is difficult to bremsstrahlung the heavy scalar, given the energy loss of the muon beam is limited. In our case, given the energy loss per penetration length is $\langle dE/dx \rangle = \mathcal{O}(10^{-2}) \text{ GeV cm}^{-1}$ and the target length is 20 cm, it will be difficult to generate scalar with mass $\gtrsim \mathcal{O}(1) \text{ GeV}$. The board range of detection sensitivity below a mass threshold is a feature of intensity experiments.

- **The left fence: SN 1987A** A crucial constraint on light scalars coupled to the Standard Model particles arises from supernova (SN) cooling. A core-collapse supernova acts like a proto-neutron star, with highly-degenerate and relativistic electrons, near-degenerate and non-relativistic nucleons, and possibly some muons [38]. It primarily cools through neutrino diffusion. The measured SN 1987A neutrino burst flux matches model predictions [39]. And the energy loss per unit mass is constrained by the so-called ‘‘Raffelt bound’’,

$$\epsilon_{\text{Raffelt}} = 10^{19} \text{ erg g}^{-1} \text{ s}^{-1}. \quad (2.13)$$

The SN event can constrain S and χ produced through prompt decays. If g_ℓ is too small, no significant dark scalar population is produced in the SN, so S does not contribute to cooling. If g_ℓ is too large, dark matter produced via S decays is trapped inside the SN and again does not contribute to cooling.

Dark scalars with mass less than the plasma frequency of the photon, ω_p ($\simeq 20 \text{ MeV}$ for SN 1987A), can be resonantly produced through mixing with the photon’s longitudinal mode [40]. See left panel of Fig. 6. Requiring the energy loss to be below this value gives an upper limit in the $m_S - g_\mu$ plane (lower edge of the excluded region) around $g_e \approx 10^{-10}$ for $m_S \lesssim 20 \text{ MeV}$ [41], translating to $g_\mu \approx 10^{-8}$. For $m_S \sim 100 \text{ MeV}$, resonant production is suppressed, but dark scalars can still be produced via continuum processes like $\gamma N \rightarrow NS$ [42]. See right panel of Fig. 6. This results in an upper limit around $g_{\gamma\gamma} \approx 6 \times 10^{-9} \text{ GeV}^{-1}$ for $m_S \lesssim 100 \text{ MeV}$ [33],

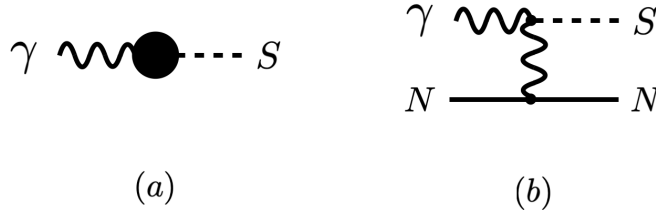


Figure 6. Processes that generate dark scalars in the SN1987A. (a) resonant mixing; Note that photons in the plasma carry an in-medium mass. Its longitude mode can mix with the scalar. (b) Primakoff process.

translating to $g_\mu \approx \text{few} \times 10^{-7}$. Dark scalars with mass above 100 MeV is too heavy to be produced in a supernova.

Once produced, dark scalars decay into $\chi\bar{\chi}$, given $m_S > 2m_\chi$ and $g_\ell \ll g_\chi = 1$. dark matter interacts with plasma particles, such as electrons, photons, and protons, limiting dark matter outflow and setting a lower limit (upper edge of the excluded region) on g_ℓ for sufficiently light scalars produced in the SN. For a rough estimate, we only consider $\chi\gamma \rightarrow \chi\gamma$ interactions and adopt a mean-free-path criterion,

$$(n_\gamma \sigma_{\chi\gamma \rightarrow \chi\gamma})^{-1} \lesssim r_{\text{core}}. \quad (2.14)$$

Adopting $n_\gamma \approx 10^{33} \text{ cm}^{-3}$ and $r_{\text{core}} \approx 1 \text{ km}$ yields $g_\mu \sim \mathcal{O}(10^{-3})$. A more sophisticated treatment uses the “ $\pi/2$ -deflection criterion” proposed by [43], leading to $g_e \approx 5 \times 10^{-7}$, translating to $g_\mu \simeq 10^{-4}$. This bound increases slightly for larger m_S as heavier dark matter is more difficult to trap.

2.5 The wall: N_{eff} constraints

BBN begins when the universe’s temperature drops below $T = \mathcal{O}(1) \text{ MeV}$ and concludes around $T = 30 \text{ keV}$. The critical stages of standard BBN include (1) neutrino decoupling, (2) n/p freeze-out, (3) electron-positron annihilation, and (4) the deuterium bottleneck. Figure 7 shows the evolution of the abundance of primordial elements during the standard BBN process [44]. These theoretical predictions are tested against observations using two key observables: the primordial ^4He mass fraction, Y_p , and the ratio of the abundances of primordial deuterium and hydrogen, D/H . The theoretical predictions for the standard BBN are [45, 46]:

$$Y_p = 0.2469 \pm 0.0002, \quad D/H = (2.506 \pm 0.110) \times 10^{-5}. \quad (2.15)$$

The current measured values are:

$$Y_p = 0.245 \pm 0.003, \quad D/H = (2.547 \pm 0.029) \times 10^{-5}. \quad (2.16)$$

Therefore, the standard BBN model is well-supported by the observational data.⁴

⁴Recent progress in addressing the overabundance of primordial ^7Li can be found in [45, 47].

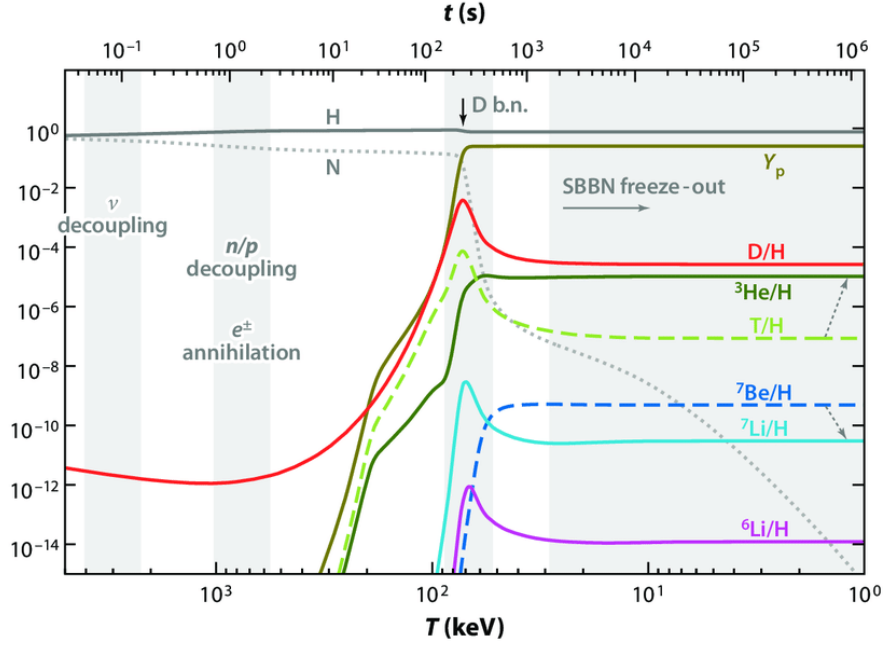


Figure 7. The evolution of the abundance of primordial elements during the standard BBN process. The gray band indicates four important stages: neutrino decoupling, n/p freeze-out and electron-positron annihilation, deuterium bottleneck, and freeze-out of all other elements. The plot is taken from [44].

BBN and CMB are crucial for constraining light dark matter and dark sector models, including those coupled to the Standard Model via dark mediators or pure gravity. The new physics is manifested in a quantity, N_{eff} , that relates the energy density of photons, ρ_γ , to the total radiation energy density, ρ_{rad} :

$$\rho_{\text{rad}} = \rho_\gamma \left(1 + \frac{7}{8} \left(\frac{4}{11} \right)^{1/3} N_{\text{eff}} \right) \Rightarrow N_{\text{eff}} \equiv \frac{8}{7} \left(\frac{11}{4} \right)^{4/3} \left(\frac{\rho_{\text{rad}} - \rho_\gamma}{\rho_\gamma} \right). \quad (2.17)$$

The pre-factor $\frac{7}{8} \left(\frac{4}{11} \right)^{1/3}$ before N_{eff} is designed explicitly for neutrinos, which were in thermal equilibrium with the Standard Model plasma until the weak interaction rate became smaller than the Hubble parameter around $T = \mathcal{O}(1)$ MeV. After decoupling, the cosmic neutrino relic undergoes expansion and maintains a quasi-thermal distribution with a temperature $T_\nu \propto a^{-1}$. Photons have the same scale-factor dependence, $T_\gamma \propto a^{-1}$. Without electron-positron annihilation, both fluids would share the same temperature.

In the standard BBN, electron-positron annihilation occurs around $T \sim 0.5$ MeV. The process heats the photons and creates an interesting ratio between T_γ and T_ν . Between neutrino decoupling and electron-positron annihilation, the total entropy degrees of freedom (dof) of the Standard Model plasma is given by (see Appendix B for more details)

$$g_{*s}(T_1) = \underbrace{2}_{\gamma\text{'s dof}} + \underbrace{\frac{7}{8}}_{\text{Fermion discount}} \left(\underbrace{2}_{e^+\text{'s dof}} + \underbrace{2}_{e^-\text{'s dof}} \right) = \frac{11}{2}. \quad (2.18)$$

After electron-positron annihilation, the total entropy dof becomes

$$g_{*s}(T_2) = \underbrace{2}_{\gamma\text{'s dof}}. \quad (2.19)$$

Entropy conservation demands

$$g_{*s}(T_1)T_1^3 = g_{*s}(T_2)T_2^3 \quad \Rightarrow \quad T_\nu = \left(\frac{4}{11}\right)^{1/3} T_\gamma, \quad (2.20)$$

where ν 's follow the temperature T_1 and γ 's follow the temperature T_2 . Therefore, if there are N_{eff} species of neutrinos, their contribution to ρ_{rad} is

$$N_{\text{eff}} \times \rho_\nu = N_{\text{eff}} \times \frac{7}{8} \left(\frac{4}{11}\right)^{4/3} \times \rho_\gamma, \quad (2.21)$$

where the photon energy density and the neutrino density (one spicity) are respectively given by

$$\rho_\gamma = 2 \times \frac{\pi^2}{30} T_\gamma^4, \quad \rho_\nu = \frac{7}{8} \times 2 \times \frac{\pi^2}{30} T_\nu^4. \quad (2.22)$$

Hence, we recover the second term in the RHS bracket of Eq. (2.17). If neutrinos decouple instantaneously, the standard BBN yields $N_{\text{eff}} = 3$. A more precise treatment of neutrino decoupling considers non-instantaneous decoupling and the process $e^+e^- \rightarrow \nu\bar{\nu}$ during the electron-positron annihilation. This yields a slightly larger value [48]

$$N_{\text{eff}}^{\text{SM}} = 3.044 \pm 0.0005. \quad (2.23)$$

If we have extra radiation sources besides photons and neutrinos, we can define

$$\Delta N_{\text{eff}} \equiv \rho_{\text{extra rad}}/\rho_\nu \quad (2.24)$$

and simplify Eq. (2.17) into

$$N_{\text{eff}} = 3.044 + \Delta N_{\text{eff}}. \quad (2.25)$$

Observationally, N_{eff} (or ΔN_{eff}) can be constrained in two ways. By carefully studying the nuclear reaction processes during BBN for different N_{eff} and comparing them to the observations of D/H and Y_p , the limit on N_{eff} from BBN [46] is given by:

$$\Delta N_{\text{eff}}^{\text{BBN}} = 0.407. \quad (2.26)$$

Note that the value is the one-sided 95% confidence level limit.

The second method relies on the CMB anisotropy. It yields the ratio $(\rho_{\text{rad}} - \rho_\gamma)/\rho_\gamma$ by measuring the angular size of the sound horizon θ_s and the angular size of the photon diffusion length θ_d [49]. The current limit from Planck 2018 (quoted from [46]) is:

$$\Delta N_{\text{eff}}^{\text{CMB}} = 0.513. \quad (2.27)$$

Again, the value is the one-sided 95% confidence level limit.

Besides anisotropy, another important measurement of CMB is the CMB temperature today, $T_{\gamma,0} = 2.73$ K, as measured by COBE/FIRAS [50]. This measurement fixes the energy density of the Standard Model electromagnetic sector ρ_γ . We would like to emphasize that $T_{\gamma,0}$ is the only temperature we have measured from the cosmological observations.

Now let us consider two examples where a light dark matter/dark sector can modify N_{eff} :

- Adding a “sterile component.” By “sterile component,” we mean any new degrees of freedom that contribute to radiation and do not inject energy into the Standard Model electromagnetic sector. This can be light dark sector particles or even stochastic gravitational waves. The effect of adding sterile components is summarized in the diagram (2.28) and is constrained by both $\Delta N_{\text{eff}}^{\text{CMB}}$ and $\Delta N_{\text{eff}}^{\text{BBN}}$.

$$\begin{aligned}
& \text{Adding sterile components} \Rightarrow \rho_{\text{rad}} \nearrow \Rightarrow N_{\text{eff}}^{\text{CMB}} \nearrow \\
& \quad \downarrow \\
& \quad H \nearrow \Rightarrow \text{Less time to burn D} \Rightarrow \text{D/H} \nearrow \\
& \quad \downarrow \\
& \quad \text{Higher } n/p \text{ freeze-out temperature} \\
& \quad \downarrow \\
& \quad Y_{\text{p}} \nearrow
\end{aligned} \tag{2.28}$$

To be more concrete, let us consider a dark sector with a real scalar S and a Dirac fermion χ . It interacts with the Standard Model sector purely gravitationally, and the two sectors conserve their entropy separately as they cool. We then have the following relation at a lower temperature,

$$a_{\text{UV}}^3 g_{\text{SM}}^{\text{UV}} T_\gamma^{\text{UV}^3} = a_{\text{IR}}^3 g_{\text{SM}}^{\text{IR}} T_\gamma^{\text{IR}^3}, \quad a_{\text{UV}}^3 g_{\text{D}}^{\text{UV}} T_{\text{D}}^{\text{UV}^3} = a_{\text{IR}}^3 g_{\text{D}}^{\text{IR}} T_{\text{D}}^{\text{IR}^3} \tag{2.29}$$

which can be combined into

$$\left(\frac{T_{\text{D}}}{T_\gamma}\right)_{\text{IR}} = \left(\frac{g_{\text{SM}}^{\text{IR}} g_{\text{D}}^{\text{UV}}}{g_{\text{SM}}^{\text{UV}} g_{\text{D}}^{\text{IR}}}\right)^{1/3} \left(\frac{T_{\text{D}}}{T_\gamma}\right)_{\text{UV}}. \tag{2.30}$$

Therefore, the energy density for the dark sector at the lower temperature is given by

$$\rho_{\text{D}}^{\text{IR}} = g_{\text{D}}^{\text{IR}} \frac{\pi^2}{30} (T_{\text{D}}^{\text{IR}})^4 = g_{\text{D}}^{\text{IR}} \frac{\pi^2}{30} \left(\frac{g_{\text{SM}}^{\text{IR}} g_{\text{D}}^{\text{UV}}}{g_{\text{SM}}^{\text{UV}} g_{\text{D}}^{\text{IR}}}\right)^{4/3} \left(\frac{T_{\text{D}}}{T_\gamma}\right)_{\text{UV}}^4 (T_\gamma^{\text{IR}})^4. \tag{2.31}$$

Consider the UV when all Standard Model particles are in the plasma and the IR before the neutrino decouples. Therefore, we have $g_{\text{SM}}^{\text{UV}} = 106.75$ and $g_{\text{SM}}^{\text{IR}} = 10.75$. For the dark sector, assume $g_{\text{D}}^{\text{UV}} = g_{\text{D}}^{\text{IR}} = g_{\text{D}}$ and that the two sectors have the same temperature at UV, $T_{\text{D}}^{\text{UV}} = T_\gamma^{\text{UV}}$. This yields

$$\rho_{\text{D}}^{\text{IR}} = g_{\text{D}}^{\text{IR}} \frac{\pi^2}{30} \times 0.047 \times (T_\gamma^{\text{IR}})^4 \Rightarrow \Delta N_{\text{eff}} = \frac{\rho_{\text{D}}^{\text{IR}}}{\rho_\nu} = 0.027 g_{\text{D}}. \tag{2.32}$$

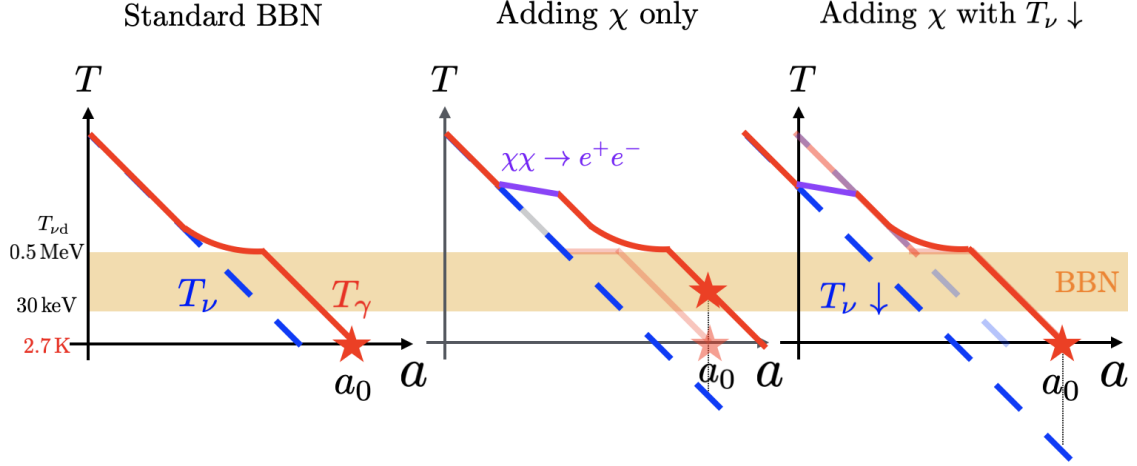


Figure 8. The evolution of the temperature of the neutrino sector T_ν and the Standard Model electromagnetic sector T_γ from before neutrino decoupling to today. Left panel: the evolution in the standard BBN, where T_γ is heated by $(11/4)^{1/3}$ due to electron-positron annihilation. The red star indicates $T_{\gamma,0}$, fixed at 2.7 K. Middle panel: adding χ that contributes to $\chi\chi \rightarrow e^+e^-$. This further heats the Standard Model electromagnetic sector, leading to a higher $T_{\gamma,0}$ than observed. Right panel: To accommodate χ , we need to lower the neutrino temperature so that $T_{\gamma,0} = 2.7$ K.

The degrees of freedom of our dark sector (S , χ , and $\bar{\chi}$) is

$$g_D = \underbrace{1}_{S\text{'s dof}} + \underbrace{\frac{7}{8}}_{\text{Fermion discount}} \left(\underbrace{2}_{\chi\text{'s dof}} + \underbrace{2}_{\bar{\chi}\text{'s dof}} \right) = \frac{9}{2} \Rightarrow \Delta N_{\text{eff}} = 0.122. \quad (2.33)$$

Such a dark sector is still allowed by current measurements of $N_{\text{eff}}^{\text{CMB}}$ and $N_{\text{eff}}^{\text{BBN}}$. If we allow asymmetric reheating such that $T_D < T_\gamma$ at UV, ΔN_{eff} from the cold dark sector is further suppressed by $(T_D/T_\gamma)^4$ and it is much easier to escape the N_{eff} constraint.

- A more interesting scenario considers dark sector particles contributing to the electromagnetic sector before BBN. Let us consider a dark matter particle χ with mass $m_\chi > m_e$, which can annihilate into e^+e^- via a dark photon. In this scenario, χ will be in chemical equilibrium with the Standard Model electromagnetic sector at high temperatures. The electromagnetic sector would be heated by $\chi\bar{\chi}$ annihilation when the temperature drops below m_χ . However, this is forbidden as it would lead to a CMB temperature today, $T_{\gamma,0}$, greater than 2.73 K, as shown in the middle panel of Fig. 8.

To accommodate the introduction of χ , we must lower the Standard Model sector temperature before the neutrino decoupling (remember $T_{\gamma,0}$ is the only temperature we measured). This results in a smaller neutrino sector temperature and restores $T_{\gamma,0}$ to the measured value. As summarized in diagram (2.34), there are still two consequences: the lower T_ν leads to lower radiation ρ_{rad} and a lower Hubble parameter during BBN, resulting in a lower $N_{\text{eff}}^{\text{CMB}}$ and lower D/H. The slower expansion of

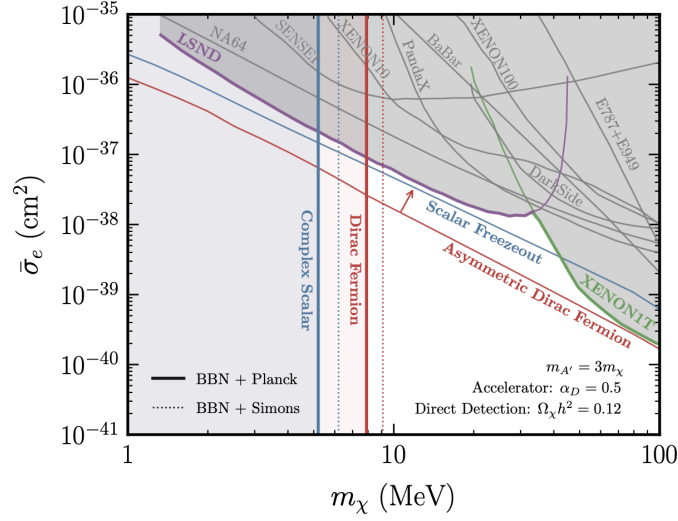


Figure 9. The constraints from N_{eff} of BBN + CMB on dark photon-dark matter model. The plot is taking from [52].

the universe allows more time for freeze-out and burns more D into heavier elements. Interestingly, Y_p is affected by two opposing factors: the lower n/p freeze-out temperature by the smaller Hubble parameter and a smaller n/p interconversion rate induced by the colder neutrino [51]. The net effect is that Y_p remains almost unchanged compared to the standard BBN.

Add χ ($\chi\chi \rightarrow e^-e^+$) \Rightarrow electromagnetic sector would be heated, but $T_{\gamma,0}$ is fixed

$$\begin{aligned}
 & \Uparrow \\
 & T_\nu \searrow \\
 & \Downarrow \\
 & \rho_{\text{rad}} \searrow \Rightarrow N_{\text{eff}}^{\text{CMB}} \searrow \\
 & \Downarrow \tag{2.34} \\
 & H \searrow \Rightarrow \text{More time to burn D} \Rightarrow \text{D/H} \searrow \\
 & \Downarrow \\
 & \text{Lower } n/p \text{ freeze-out temperature} \\
 & \text{But } T_\nu \searrow \Rightarrow \text{Less } n/p \text{ interconversion rate} \\
 & \Downarrow \\
 & Y_p \text{ unchanged}
 \end{aligned}$$

One may think of hiding the extra annihilation by adding sterile components. In this case, the changes in $N_{\text{eff}}^{\text{CMB}}$ and D/H cancel. However, the enhancement in Y_p cannot be mitigated unless additional new physics is introduced. See diagram (2.35). Since

Y_p alone is well-measured, we still have strong constraints on χ .

$$\begin{aligned}
& \text{Add } \chi \ (\chi\chi \rightarrow e^-e^+) \text{ and sterile components} \Rightarrow N_{\text{eff}}^{\text{CMB}} \text{ unchanged} \\
& \quad \Downarrow \\
& \text{D/H unchanged, but } Y_p \nearrow
\end{aligned} \tag{2.35}$$

The quantitative analysis of the extra annihilation scenario, the combined scenario, or other more involved non-standard BBN scenarios requires implementing the nuclear reaction processes using BBN codes, such as ACROPOLIS [53], ALTERBBN [54], PRIMAT [55, 56], and PRYMORDIAL [57]. Ref. [52] considers a dark sector with a dark photon A' and a complex scalar or Dirac fermion dark matter χ . Using a modified PRIMAT code, the authors set $m_\chi > 5.2(7.9)$ MeV for dark matter to be a complex scalar (Dirac fermion), assuming the mass ratio $m_{A'}/m_\chi = 3$. This is shown as the left “walls” in Fig. 9. The bound is valid as long as the coupling between the dark matter and the Standard Model sector is large enough to bring $\chi\chi \leftrightarrow e^+e^-$ to chemical equilibrium when $T_\gamma \gtrsim m_{A'}$, i.e., $(\Gamma_{\chi\chi \leftrightarrow e^+e^-} = H)_{T_\gamma=m_{A'}}$. The result corresponds to $\bar{\sigma}_e \equiv \frac{16\pi\alpha\alpha_D\epsilon^2\mu_{\chi e}^2}{(\alpha^2 m_e^2 + m_{A'}^2)^2} \gtrsim 10^{-43} \text{ cm}^2$.

3 Second lecture

There is a bloom of dark matter models in the particle physics community. But many models lead to similar predictions in the astrophysical observations and can be summarized in a few baseline models. Besides CDM, the baseline models are

- Warm dark matter (WDM)
- Fuzzy dark matter (FDM), a.k.a., ultralight dark matter
- Self-interacting dark matter (SIDM)
- Interacting dark matter (IDM)

WDM primarily affects the halo mass function. FDM also alters the halo mass function but, in addition, leads to very different dark matter density profiles within the halos. SIDM does not modify the halo mass function but results in dynamically evolving dark matter density profiles within the halos. IDM involves strong interactions with baryons, with cross-sections surpassing those of dark matter overburden. IDM can produce a halo mass function similar to WDM and additional features such as dark acoustic oscillations. Some dark matter models combine features from multiple baseline models. An example is atomic dark matter, consisting of dark electrons, protons, and photons. Its phenomenology exhibits characteristics of WDM, SIDM, and IDM.

The popularity of these baseline models is due to two main reasons. Firstly, dark matter on a large scale is well-constrained and is expected to be CDM-like. Consequently, significant deviations are anticipated only in the small-scale structures, i.e., dark matter halos. Secondly, astrophysical and cosmological studies often require extensive numerical

simulations. Thus, models with a single parameter, such as dark matter mass for WDM and FDM or cross-section strength for SIDM, are ideal. However, new techniques like machine learning may allow us to thoroughly explore models with multiple parameters, such as IDM and atomic dark matter.

In the following sections, we will discuss two aspects of beyond-CDM imprints on small-scale structures: the effects on structure formation, which influence the distribution of halos of various masses, and the effects on a single halos' density profiles.

3.1 Small-scale power spectrum: probing dark matter in the early universe

Our universe today is full of matter-rich halos and matter-poor voids, which respectively developed from small initial overdensities and under densities in the primordial matter distribution. These overdensities, denoted by

$$\delta_{\text{m}}(\mathbf{x}) \equiv \frac{\rho_{\text{m}}(\mathbf{x}) - \bar{\rho}_{\text{m}}}{\bar{\rho}_{\text{m}}}, \quad (3.1)$$

where $\bar{\rho}_{\text{m}}$ is the averaged matter density, grows over time due to gravity. Specifically, they first grew in the linear perturbation regime, where $\delta_{\text{m}} \ll 1$, as the long-wavelength modes re-entered the horizon. As these overdensities evolved, they entered the non-linear regime ($\delta_{\text{m}} > 1$), leading to the collapse of surrounding background dark matter and the formation of virialized halos. The average density of a dark matter halo is approximately $\Delta = 200$ times the background density. Smaller halos merged or accreted matter to form larger ones, a process manifested in the halo mass-redshift relation and the concentration-halo mass-redshift relation, with concentration indicating how compact a halo is.

In practice, we use “two-point statistics,” i.e., the matter power spectrum and the halo mass function, to characterize the distributions of overdensities and halos, respectively. These tools are essential for studying the properties of dark matter and beyond. While large-scale observations generally support the predictions of Λ CDM, there can be significant deviations on smaller scales. Additionally, observations of galaxies and dwarf galaxies have raised several challenging questions for Λ CDM, such as the diversity of rotation curves and the too-big-to-fail problem, which suggests the need for dark matter models beyond CDM.

Like dealing other types of fields, it is better to analyze the overdensity field in the momentum space than the position space. The two representations are related by the Fourier transform:

$$\delta_{\text{m}}(\mathbf{x}) = \int d^3k \delta_{\text{m}}(\mathbf{k}) e^{-i\mathbf{k}\cdot\mathbf{x}}, \quad (3.2)$$

where \mathbf{k} is the 3D momentum vector. The matter power spectrum, P_{m} , is related to the two-point correlation function of $\delta_{\text{m}}(\mathbf{k})$ by:

$$\langle \delta_{\text{m}}(\mathbf{k}) \delta_{\text{m}}(\mathbf{k}') \rangle = (2\pi)^3 \delta^3(\mathbf{k} + \mathbf{k}') P_{\text{m}}(k) \quad (3.3)$$

where $\langle \dots \rangle$ averages over all the spacial configurations and P_{m} is only a function of the magnitude of \mathbf{k} due to the cosmological principle. Often it is convenient to introduce dimensionless matter power spectrum $\Delta^2(k)$ that relates to $P_{\text{m}}(k)$ by

$$\Delta^2(k) \equiv \frac{k^3 P_{\text{m}}(k)}{2\pi^2}. \quad (3.4)$$

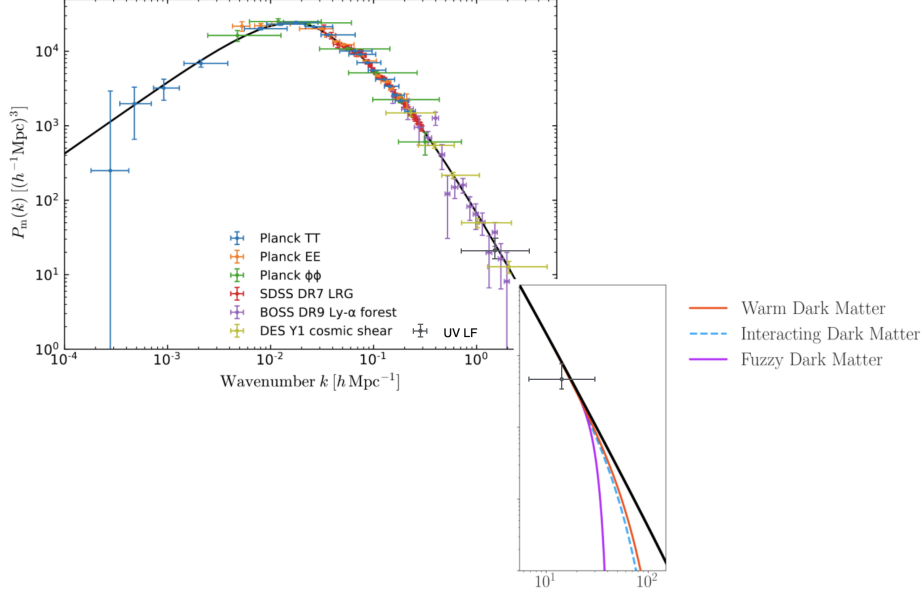


Figure 10. Linear matter power spectrum at $z = 0$, reproduced from Nadler’s BCCP seminar slides [58]. We added constraints from the ultraviolet galaxy luminosity function (UV LF) [59]. The measured data are complied by [60]. From the largest scales to smaller ones, the data includes Planck CMB, galaxy clustering, galaxy weak lensing, Ly- α clustering, and UV LF.

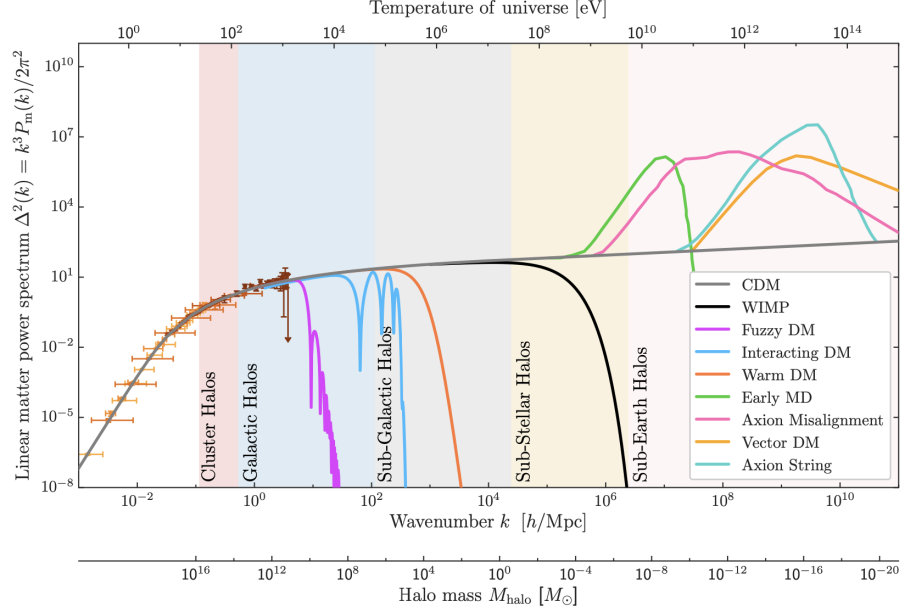


Figure 11. Dimensionless linear matter power spectrum at $z = 0$, reproduced from [61]. A detailed explanation of model predictions can be found in [61]. The measured data are complied by [60].

Fig. 10 (Fig. 11) shows the (dimensionless) linear matter spectrum at $z = 0$ for the CDM, WDM, FDM, and IDM, along with observations from CMB and LSS. As is common in astronomical plots, the data should be read from right to left. Modes with smaller

wavenumbers enter the horizon earlier than those with larger wavenumbers. First, let us focus on the CDM prediction, which sets the baseline of the matter power spectrum that agrees well with observations at $k \lesssim 10 h \text{ Mpc}^{-1}$.

3.1.1 The power spectrum of CDM

A notable feature of the CDM power spectrum is the turnover around $k = 0.02 h \text{ Mpc}^{-1}$. This scale corresponds to modes entering the horizon at the matter-radiation equality, denoted as k_{eq} . For modes with wavenumber $k < k_{\text{eq}}$, the power spectrum behaviors as $P_{\text{m}}(k) \propto k$. For modes with wavenumber $k > k_{\text{eq}}$, the relationship changes to $P_{\text{m}}(k) \propto k^{-3}$. In the dimensionless spectrum, where $P_{\text{m}}(k)$ is multiplied by k^3 , we find $\Delta^2(k) \propto k^4$ for $k < k_{\text{eq}}$, and $P_{\text{m}}(k)$ exhibits a logarithmic-like growth with respect to k for $k > k_{\text{eq}}$.

The turnover behaviour can be well explained using the linear perturbation theory of the Einstein-Boltzmann equation. A more detailed and comprehensive derivation can be found in works such as [3], which starts by perturbing a set of fluid dynamics equations:

$$\frac{\partial \rho}{\partial t} + \nabla \cdot (\rho \mathbf{u}) = 0, \quad \frac{\partial \mathbf{u}}{\partial t} + (\mathbf{u} \cdot \nabla) \mathbf{u} = -\nabla \Phi - \frac{\nabla P}{\rho}, \quad \nabla^2 \Phi = 4\pi G \rho, \quad (3.5)$$

where ρ , P , and \mathbf{u} is the fluid's density, pressure, and velocity and Φ is the gravitational potential. Here, we simplify the derivation by directly introducing the resulting master equation:

$$\frac{d^2 \delta_{\text{m}}}{dt^2} + 2H \frac{d\delta_{\text{m}}}{dt} = 4\pi G \bar{\rho}(t) \delta_{\text{m}}, \quad (3.6)$$

where we assume that the matter has zero pressure and all the matter clumps. Although this assumption is not entirely accurate, it is not far off and simplifies our derivation. To solve the master equation, we use the ansatz

$$\delta_{\text{m}}(\mathbf{k}, t) = \delta_+(\mathbf{k}) D_+(t) + \delta_-(\mathbf{k}) D_-(t), \quad (3.7)$$

to separate the \mathbf{k} -dependent and t -dependent parts of δ_{m} . The subscript “+” refers to the growing mode, and “−” to the decaying mode. We will focus on the growing mode, which leads to the large matter perturbation in the later universe.

In the matter era, we have $a \propto t^{2/3}$, $H = 2/(3t) \propto a^{-3/2}$, and $4\pi G \bar{\rho}_{\text{m}}(t) = 3H^2/2 = 2/(3t^2)$ (see Tab. 4 for a summary). Substituting those relations to Eq. (3.6) yields

$$\frac{d^2 D}{dt^2} + \frac{4}{3t} \frac{dD}{dt} = \frac{2}{3t^2} D \quad \Rightarrow \quad D(t) = c_1 t^{-1} + c_2 t^{2/3}, \quad (3.8)$$

where c_i 's are constants. From the solution, we find that the growing mode gives $D_+ \propto t^{2/3} \propto a$.

In the radiation era, the scale factor behaves as $a \propto t^{1/2}$, and the Hubble parameter is given by $H = 1/(2t) \propto a^{-2}$. In such a universe,

$$\ddot{\delta}_{\text{m}} \sim H \dot{\delta}_{\text{m}} \sim H^2 \delta_{\text{m}} \sim 4\pi G (\bar{\rho}_{\text{rad}} + \bar{\rho}_{\text{m}}) \delta_{\text{m}} \gg 4\pi G \bar{\rho}_{\text{m}} \delta_{\text{m}}, \quad (3.9)$$

so the right-hand side of Eq. (3.6) can be approximated as zero:

$$\frac{d^2 D}{dt^2} + \frac{1}{t} \frac{dD}{dt} = 0 \quad \Rightarrow \quad D(t) = c_1 + c_2 \ln t. \quad (3.10)$$

Therefore, the growing mode in this era gives $D_+ \propto \ln t \propto \ln a$.

The above results suggest that sub-horizon fluctuations in the radiation era only grow logarithmically, or approximately $\delta_m \sim \text{const}$, while in the matter era, the growth accelerates to $\delta_m \propto a$. This difference in growth rates leads to the k -dependence in the matter power spectrum. This is because different k -modes re-enter the horizon at different times in different eras, experiencing different sub-horizon growth. Let us look at it in more detail.

Many inflation models suggest that the initial matter power spectrum is scale-invariant. This means

$$(k^3 P_m)_i = \text{const}. \quad (3.11)$$

Modes outside the horizon always have the same shape as the initial spectrum. Now consider modes re-entering the horizon during the matter era, their amplitudes grow by (a_0/a_h) , where a_0 is the scale factor today (ignoring the dark energy era) and a_h is the scale factor at horizon re-entering. In the matter era, a_h is determined by

$$k = a_h H(a_h) \propto a_h a_h^{-3/2} \Rightarrow a_h \propto k^{-2}. \quad (3.12)$$

Therefore, the power spectrum is scaled as

$$k^3 P_m \propto \left(\frac{a_0}{a_h}\right)^2 (k^3 P_m)_i \propto k^4. \quad (3.13)$$

The square over (a_0/a_h) is because $P_m \propto \delta_m^2$.

For modes crossing the horizon during the radiation era, their amplitudes grow by $\ln(a_{\text{eq}}/a_h)$, where a_{eq} is the scale factor at matter-radiation equality. a_h in the radiation era is given by

$$k = a_h H(a_h) \propto a_h a_h^{-2} \Rightarrow a_h \propto k^{-1}. \quad (3.14)$$

This leads to the power spectrum scaling

$$k^3 P_m \propto \left(\ln \frac{a_{\text{eq}}}{a_h}\right)^2 (k^3 P_m)_i \propto \left(\ln \frac{k}{k_{\text{eq}}}\right)^2. \quad (3.15)$$

Note that when those modes are later involved in the matter era, their amplitude will be enhanced by a common factor that does not affect the shape of the spectrum. Combining the above results, we have the k -dependence

$$P_m(k) \propto \begin{cases} k & k < k_{\text{eq}}, \\ k^{-3} \left(\ln \frac{k}{k_{\text{eq}}}\right)^2 & k > k_{\text{eq}}. \end{cases} \quad (3.16)$$

The evolution of the power spectrum's shape for different cosmological eras is depicted in Fig. 12.

3.1.2 The power spectrum of dark matter beyond CDM

Many dark matter models beyond CDM can suppress the power spectrum at small scales. Because the matter power spectrum $P_m(k)$ is related to the halo mass function $\frac{dN}{dM_h}(M_h)$, by

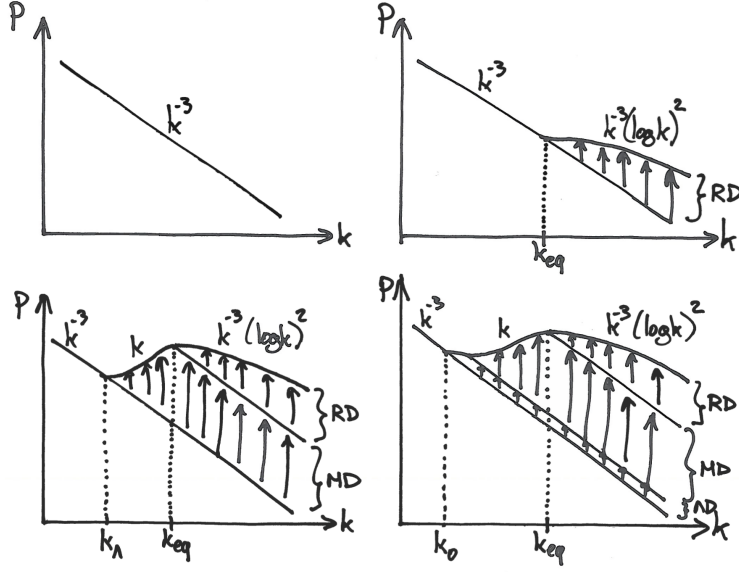


Figure 12. How the shape of the matter power spectrum evolves in time. The four panels correspond to the initial spectrum, the spectra at the radiation era, matter era, and dark energy era, respectively. The figure is taken from [62].

carefully observing galaxies and dwarf galaxies, we have an opportunity to detect deviations from the CDM model and learn more about the properties of dark matter. In addition, because the small-scale structures began to grow in the radiation era, new physics that suppressed them should be active during the period. Therefore, the small-scale structure provides us a window to probe dark matter in the early universe.

Now, let us focus on a few examples:

1. Warm Dark Matter: The comoving wavelength for free-streaming is given by

$$\lambda_{\text{fs}} = \int_{t_i}^{t_{\text{eq}}} dt \frac{\langle v(t) \rangle}{a(t)}, \quad k_{\text{fs}} = \frac{2\pi}{\lambda_{\text{fs}}}, \quad (3.17)$$

where $\langle v(t) \rangle$ is the physical velocity averaging over the WDM's phase space. Note that the integral extends from an initial time t_i to the matter-radiation equality. Beyond the matter-radiation equality, the Jeans' length drops dramatically, and perturbations could collapse under gravity. A crude estimation finds [63]

$$\lambda_{\text{fs}} = \int_0^{t_{\text{NR}}} dt \frac{c}{a(t)} + \int_{t_{\text{NR}}}^{t_{\text{eq}}} dt \frac{ca_{\text{NR}}}{a^2(t)} = r_{\text{H}}(t_{\text{NR}}) \left(1 + \frac{1}{2} \ln \frac{t_{\text{eq}}}{t_{\text{NR}}} \right), \quad (3.18)$$

where $r_{\text{H}}(t_{\text{NR}})$ is the comoving horizon at t_{NR} . The WDM moves at the speed of light c before t_{NR} and slows down as a^{-1} between t_{NR} and t_{eq} . Choosing t_{NR} to be the temperature $T_{\text{WDM}} = m_{\text{WDM}}/3$ yields

$$\lambda_{\text{fs}} = 0.4 \left(\frac{m_{\text{WDM}}}{\text{keV}} \right)^{-4/3} \left(\frac{\Omega_{\text{WDM}} h^2}{0.135} \right)^{1/3} h^{-1} \text{Mpc}. \quad (3.19)$$

This free-streaming comoving wavelength sets a cutoff on the dark matter halo mass:

$$M_{\text{cut}} = \frac{4\pi}{3} \rho \left(\frac{\pi}{k_{\text{fs}}} \right)^3 = \frac{4\pi}{3} \rho \left(\frac{\lambda_{\text{fs}}}{2} \right)^3, \quad (3.20)$$

where ρ is the dark matter density. Below this cutoff, we do not expect to observe any halos because the free-streaming washouts the density perturbation.

Stronger constraints on WDM can be obtained by realizing that the removal of smaller halos can affect the properties of larger halos with masses above M_{cut} , causing a departure from the observed halo mass function. This is because larger halos grow out of smaller halos according to hierarchical structure formation. The halo mass function is closely related to the linear matter power spectrum. However, the exact relation is non-trivial, and one needs to run cosmological simulations to pinpoint it. Fortunately, WDM is one of the beyond-CDM models that has been intensively studied in the simulation community (thanks to the resolved “missing satellite problem”). Based on simulation results, Ref. [64, 65] finds that the power spectrum of WDM relative to CDM is given by

$$\frac{P_{\text{WDM}}(k)}{P_{\text{CDM}}(k)} = [1 + (\alpha k)^{2\nu}]^{-\frac{10}{\nu}}, \quad (3.21)$$

with $\nu = 1.12$ and

$$\alpha = 0.049 \left(\frac{m_{\text{WDM}}}{\text{keV}} \right)^{-1.11} \left(\frac{\Omega_{\text{WDM}}}{0.25} \right)^{0.11} \left(\frac{h}{0.7} \right)^{1.22} h^{-1} \text{Mpc}, \quad (3.22)$$

where m_{WDM} and Ω_{WDM} are the WDM mass and abundance, respectively. Also note that

$$\frac{P_{\text{beyond CDM}}(k)}{P_{\text{CDM}}(k)} = [1 + (\alpha k)^\beta]^\gamma, \quad (3.23)$$

is the common functional form used to parameterize the power spectrum for beyond-CDM dark matter, which guarantees $P_{\text{beyond CDM}}/P_{\text{CDM}} = 1$ for $k \rightarrow 0$.

2. Fuzzy dark matter: FDM is naturally associated with the de Broglie wavelength scale of the ultralight dark matter,

$$\lambda_{\text{dB}} = \frac{1}{m_{\text{FDM}} v}. \quad (3.24)$$

This scale is linked to the soliton size at the center of an FDM halo. We are interested in the gravitational instability scale and the halo mass cutoff of FDM. This process is naturally associated with the Jeans scales of FDM. The derivation of the Jeans scale starts from the fluid description of FDM, also known as the Madelung equations [66],

$$\frac{\partial \rho}{\partial t} + \nabla \cdot (\rho \mathbf{u}) = 0, \quad \frac{\partial \mathbf{u}}{\partial t} + (\mathbf{u} \cdot \nabla) \mathbf{u} = -\nabla \Phi + \frac{\hbar^2}{2m_{\text{FDM}}^2} \nabla \left(\frac{\Delta \sqrt{\rho}}{\sqrt{\rho}} \right), \quad \nabla^2 \Phi = 4\pi G(\rho - \bar{\rho}), \quad (3.25)$$

where we assume FDM is pressureless. Perturbing these equations around a homogeneous distribution ($\rho = \bar{\rho}$, $\mathbf{v} = 0$, $\Phi = 0$) yields,

$$\frac{\partial^2}{\partial t^2} \delta_{\text{m}} = 4\pi G \bar{\rho} \delta_{\text{m}} - \frac{\hbar^2 k^4}{4m_{\text{FDM}}^2} \delta_{\text{m}}. \quad (3.26)$$

This equation is similar to Eq. (3.6) except for the absence of Hubble friction and the appearance of the “quantum pressure” term. The solution of Eq. (3.26) is given by

$$\delta_m(t) = c_1 \exp \left(t \sqrt{4\pi G \rho - \frac{\hbar^2 k^4}{4m_{\text{FDM}}^2}} \right) + c_2 \exp \left(-t \sqrt{4\pi G \rho - \frac{\hbar^2 k^4}{4m_{\text{FDM}}^2}} \right) \quad (3.27)$$

The Jeans wavenumber corresponds to the critical value of k that allows the perturbation to grow with time. It is set by

$$k_J = \frac{2\pi^{1/4} G^{1/4} \rho^{1/4} m_{\text{FDM}}^{1/2}}{\hbar^{1/2}}, \quad \lambda_J = \frac{2\pi}{k_J}. \quad (3.28)$$

Modes with $k > k_J$ are suppressed due to the quantum pressure. The halo cutoff mass is given by [17]

$$M_{\text{cut}} = \frac{4}{3} \pi \rho \left(\frac{\lambda_J}{2} \right)^2 = 1.5 \times 10^7 M_\odot \left(\frac{\Omega_{\text{FDM}}}{0.27} \right)^{1/4} \left(\frac{h}{0.7} \right)^{1/2} \left(\frac{10^{-22} \text{ eV}}{m_{\text{FDM}}} \right)^{3/2} \quad (3.29)$$

Similar to the WDM case, stronger constraints can be obtained by considering the departure from the CDM power spectrum, i.e., the imprint of FDM on larger halos. Using an emulator, analysis of the Lyman- α forest constrains $m_{\text{FDM}} > 2 \times 10^{-20}$ eV [67].

3. Interacting Dark Matter: The gravitational instability scale for IDM is determined by the horizon size, R_H , at the moment when dark matter and Standard Model particles kinetically decouple.

$$\lambda_{\text{kd}} = R_H(\mathcal{R}_{\text{kd}} = H), \quad (3.30)$$

where \mathcal{R}_{kd} is the kinetic decoupling rate, and we use $\chi - p$ interactions as an example to illustrate the derivation. Similar kinetic decoupling processes apply to other dark matter-Standard Model interactions, such as $\chi - e$ interactions. Only modes with wavelengths greater than λ_{kd} can gravitational collapse to form halos. Modes with $\lambda < \lambda_{\text{kd}}$ are suppressed due to the strong interactions which transfer extra random motions from the Standard Model fluid to the dark matter fluid. For a single $2 \rightarrow 2$ elastic scattering process, the dark matter particle with velocity \mathbf{v}_χ will experience a velocity change of

$$\Delta \mathbf{v}_\chi = \frac{m_p}{m_\chi + m_p} v_{\text{rel}} \left(\hat{\mathbf{n}}_\chi - \frac{\mathbf{v}_{\text{rel}}}{v_{\text{rel}}} \right), \quad (3.31)$$

where $\hat{\mathbf{n}}_\chi$ is the direction of the scattered dark matter particle in the center-of-mass frame. The peculiar velocity of the dark matter fluid, \mathbf{V}_χ , is then given by

$$\frac{d}{dt} \mathbf{V}_\chi = n_\chi \langle \sigma_{\chi p \rightarrow \chi p} v_{\text{rel}} \Delta \mathbf{v}_\chi \rangle = -\mathcal{R}_{\text{kd}} (\mathbf{V}_\chi - \mathbf{V}_p), \quad \mathcal{R}_{\text{kd}} \simeq \frac{m_p}{m_\chi + m_p} n_p \sigma_{\chi p \rightarrow \chi p} v_{\text{rel}} \quad (3.32)$$

where $\langle \cdot \rangle$ denotes averaging over all scattering angles and the velocity distributions of dark matter and protons.

The complete derivation of λ_{kd} is more involved. Dark matter and protons are initially fully coupled, then thermally decoupled, and finally kinetically decoupled. During the period between thermal and kinetic decoupling, the temperature of dark matter evolves as $T_\chi \propto a^{-2}$, which differs from the Standard Model plasma's evolution $T_\gamma \propto a^{-1}$. Therefore, it is necessary to first determine the scale factor at thermal decoupling a_{td} and then link it to the scale factor at kinetic decoupling a_{kd} . For more details, see [68].

Again, better constraints can be obtained through cosmological simulations from the IDM's initial linear power spectrum. However, this involves running simulations to scan over m_χ and $\sigma_{\chi p}$ and can be costly. An alternative way to constrain IDM is by comparing its power spectrum to that of WDM with the maximally allowed m_{WDM} . Such a procedure is allowed because the spectra of WDM and IDM are similar. One can constrain IDM by requiring $P_{\text{IDM}}(m_{\text{IDM}}, \sigma_{\chi p})/P_{\text{CDM}}$ to always lie below $P_{\text{WDM}}(m_{\text{WDM}}^{\text{limit}})/P_{\text{CDM}}$. For more details, see [68].

3.1.3 Observations

There is a correspondence between modes with comoving wavenumber k and the mass of the halo systems, which follows the relation:

$$M_{\text{h}} \simeq \frac{4\pi}{3} \rho_{\text{m}} \left(\frac{\pi}{k} \right)^3 \simeq 10^{10} M_\odot \left(\frac{10 h \text{ Mpc}^{-1}}{k} \right)^3. \quad (3.33)$$

Thus, we have three important observational targets for different values of k :

1. $k \sim 0.1 - 1 h \text{ Mpc}^{-1}$: galaxy cluster halos;
2. $k \sim 1 - 100 h \text{ Mpc}^{-1}$: galaxy halos;
3. $k \gtrsim 100 h \text{ Mpc}^{-1}$: completely dark halos whose gravitational potential is too shallow to form galaxies.

Probing the matter power spectrum at small scales requires finding methods to robustly investigate dark matter halos at those scales. For galaxy cluster halos, we can probe them by tracing hydrogen distribution using the Lyman- α forest, where light from distant quasars is absorbed by intergalactic neutral hydrogen residing inside halos. For galaxy halos, we can infer their abundance by observing luminous Milky Way satellite galaxies through the “galaxy-halo connection”. For completely dark halos, we must rely on other methods, such as strong gravitational lensing or stellar streams.

To showcase the potential of different probes, we present the limits on WDM inferred from various methods or their combinations in Tab. 2 and show the parameter space constraints on IDM in Fig. 13 (taken from [68]). As shown in Fig. 13, the resulting constraints from the Milky Way satellite and Lyman- α on $\sigma_{\chi p(\chi e)}$ cover a wide range of m_χ . It almost rules out all large values for the dark matter overburden scenario, where the null detection of dark matter in underground direct detection experiments is due to the strong interactions between dark matter and the Earth's atmosphere and rocks. The result clearly shows that the cosmological probes complement direct detection experiments and other dark matter-dark sector probes.

Ref.	Data type	$m_{\text{WDM}}^{95\% \text{C.L.}}$ [keV]	h	Ω_{dm}
[69]	luminous satellite galaxies	3.26	0.67	0.265
[70]	luminous satellite galaxies	6.5	0.7	0.24
[71]	luminous satellite galaxies	2.02	0.7	0.23
[72]	stellar stream, luminous satellite galaxies	6.3	0.67	0.26
[73]	strong lensing, luminous satellite galaxies	9.7	0.7	0.24
[74]	strong lensing, luminous satellite galaxies, Lyman- α	6.733	0.7	0.25

Table 2. 95% C.L. lower limits on the WDM mass (3rd column) from MW subhalo data reported in the literature. The 2nd, 4th, and 5th columns respectively show the data type, the value of h , and the value of Ω_{dm} that was used in the derivation of the limits.

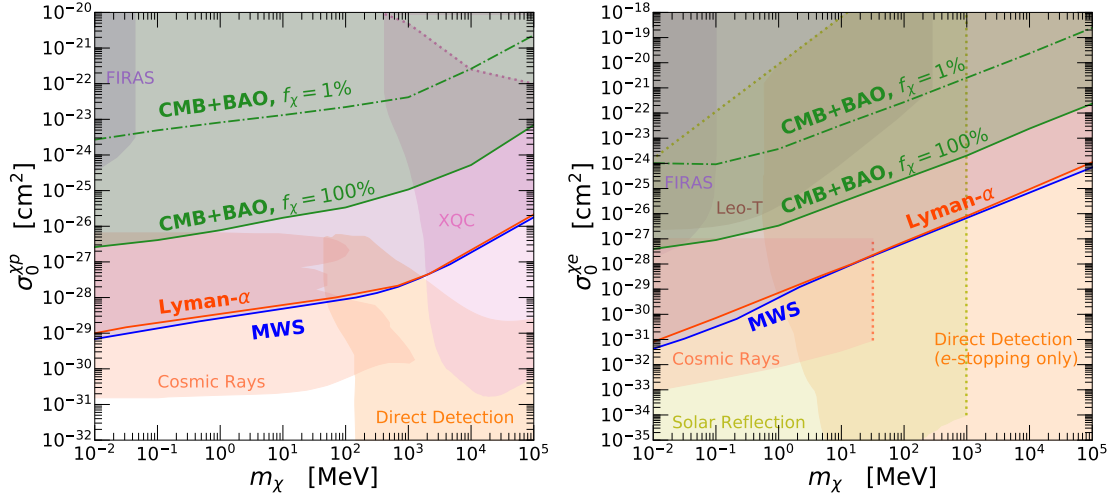


Figure 13. 95% C.L. bounds from MW subhalos (solid blue), Lyman- α forest (solid red), CMB+BAO (solid green) datasets, for velocity-independent (left) dark matter–protons and (right) dark matter–electron interactions. We also include constraints from previous literature. For dark matter–proton interactions (left): XQC rocket (pink) [75–77], various direct-detection experiments (orange: CRESST-III [78, 79], CRESST surface run [80], XENON1T [81], and Migdal effect-based EDELWEISS [82]), and cosmic-ray accelerated dark matter [83] (coral red: Mini-BOONE and XENON1T [84]; and Daya Bay and KamLAND [85]). For dark matter–electron interactions (right): gas cooling of Leo-T dwarf galaxy (brown) [86], various direct-detection experiments as considered in [87] (orange: XENON10 [88–90], XENON100 [89, 91], DarkSide-50 [92], CDMS-HVev [93], protoSENSEI [94, 95], and SENSEI at MINOS [96]); cosmic-ray accelerated dark matter (coral red: Super-K and MiniBooNE [85, 97]), and bounds from solar reflection (yellow) [98, 99]. The dotted lines represent our conservative assumptions about the limits of the XQC (pink, with the ceiling from [76]); cosmic-ray (coral red [97]), and solar reflection (yellow [99]) bounds. In both panels: FIRAS (purple) [100–102].

3.2 Inside dark matter halos: self-interacting dark matter

CDM encountered several challenges at small scales, including the core vs. cusp problem, the diversity problem, and the too-big-to-fail problem (see review by [103]). SIDM offers a common solution by providing an intrinsic mechanism to alter the dark matter distribution

within halos. The core formed during the early gravothermal evolution in SIDM can address both the core vs. cusp and too-big-to-fail problems. Additionally, the super-cuspy profile that develops in the late core-collapse stage, along with the early-stage core, may resolve the full scope of the diversity problem.

3.2.1 A qualitative understanding

The behavior of self-interacting dark matter (SIDM) at different stages can be understood, at the zeroth order, using the hydrostatic equation:

$$\frac{\nabla P}{\rho} = -\nabla\Phi, \quad (3.34)$$

where $P \equiv \rho\nu^2$ is the SIDM pressure, ν is the one-dimensional velocity dispersion, and Φ is the gravitational potential of the halo. Under spherical symmetry, this equation can be rewritten as:

$$\frac{\partial(\rho\nu^2)}{\partial r} = -\frac{GM(<r)\rho}{r^2}, \quad (3.35)$$

where $M(<r)$ is the enclosed mass.

Let us consider the density profile at the time of halo formation. Since the dynamical time of a halo is typically much shorter than the SIDM relaxation time, the density profile at halo formation will be similar to that of CDM halo, i.e., the NFW profile:

$$\rho(r) = \frac{\rho_s}{(r/r_s)(1+r/r_s)^2}, \quad (3.36)$$

where ρ_s and r_s are the scale density and radius, respectively. For the inner halo region, the density scales as $\rho \propto r^{-1}$. Therefore, $M \propto r^2$. Assuming $\nu \propto r^s$, the left-hand side (LHS) and right-hand side (RHS) of Eq. (3.35) respectively scale as:

$$\text{LHS} \propto \frac{r^{-1}r^{2s}}{r} = r^{2s-2}, \quad \text{RHS} \propto \frac{r^2r^{-1}}{r^2} = r^{-1}. \quad (3.37)$$

Requiring the LHS and RHS to have the same scaling behavior gives:

$$2s - 2 = -1 \quad \Rightarrow \quad s = \frac{1}{2}. \quad (3.38)$$

$\nu \propto r^{1/2}$ means the halo will be cold at the center and hot at the scale radius. Such initial temperature imbalance creates an opportunity for SIDM to manifest its effect—thermalizing regions with different temperatures.

Next, let us consider the end result of the self-interactions — the isothermal limit, where ν is independent of r . In this case, we can move ν^2 out of the partial derivative on the LHS of Eq. (3.35) and rewrite the equation as:

$$\frac{\partial \ln \rho}{\partial \ln r} = -\frac{GM(<r)}{r\nu^2}. \quad (3.39)$$

There are two scenarios to consider:

1. **Finite central density:** $\lim_{r \rightarrow 0} \rho = \rho_0$. In this case, $\lim_{r \rightarrow 0} M = \frac{4\pi}{3} \rho_0 r^3$ and ν is independent of r , therefore $\lim_{r \rightarrow 0} \text{RHS} = 0$. This leads to $\lim_{r \rightarrow 0} \frac{\partial \ln \rho}{\partial \ln r} = 0$, which means the isothermal profile can have a flat core.
2. **Single power law (with infinite central density):** we assume the density follows the ansatz $\rho = Ar^x$. Substituting it into Eq. (3.39) gives:

$$x = -\frac{4\pi G}{3} Ar^{x+2} \nu^{-2} \Rightarrow x = -2, A = \frac{3\nu^2}{2\pi G} \Rightarrow \rho = \frac{3\nu^2}{2\pi G r^2}. \quad (3.40)$$

This is the so-called singular isothermal profile. Note that this is one solution but not the only solution of Eq. (3.39).

Therefore, a SIDM model, which obeys Eq. (3.39), is capable to produce both a cored profile and an isothermal profile. More detailed analysis shows that the density profile in the inner part of a core-collapsed halo (outside the secondary core) scales as $r^{-2.2}$. The slight deviation from r^{-2} is significant because the density slope is related to the velocity dispersion slope by

$$\frac{d \ln \nu}{d \ln r} = 1 + \frac{1}{2} \frac{d \ln \rho}{d \ln r}, \quad (3.41)$$

which can be again derived from the hydrostatic equation (left as an exercise). Therefore,

$$\frac{d \ln \rho}{d \ln r} < -2 \Rightarrow \frac{d \ln \nu}{d \ln r} < 0. \quad (3.42)$$

A negative velocity dispersion gradient means heat outflows from the core of the halo to its outskirts. The process is necessary for SIDM to evolve from a cored phase to a core collapsed phase. Unlike typical thermal systems, an SIDM halo, viewed as a gravothermal system, has a negative heat capacity. The heat outflow *heats* the core and generates more heat outflow, and the system's maximum entropy is infinite, leading to a core-collapsed halo.

The evolution time from the initial NFW profile to the cored profile and then to the quasi-isothermal profile depends on the relaxation time of dark matter self-interaction. The relaxation time is typically given by

$$t_{\text{rlx}} = \frac{1}{n\sigma v} = \frac{1}{\rho(\sigma/m)v} = 1.5 \text{ Gyr} \left(\frac{0.4 \text{ GeV cm}^{-3}}{\rho} \right) \left(\frac{1 \text{ cm}^2 \text{ g}^{-1}}{\sigma/m} \right) \left(\frac{300 \text{ km s}^{-1}}{v_{\text{rel}}} \right). \quad (3.43)$$

Simulations show that it takes $t = \mathcal{O}(1) \times t_{\text{rlx}}$ for the halo to evolve from the initial NFW profile to the cored profile, and $t = \mathcal{O}(100) \times t_{\text{rlx}}$ for the halo to further evolve to the quasi-isothermal profile. Note that this evolution time is strongly influenced by the halo properties, in particular the halo concentration c_h , defined as the halo radius r_h over the scale radius r_s of the initial halo profile. In summary, SIDM halos can exhibit NFW, cored, or quasi-isothermal profiles depending on their evolution time and halo properties.

3.2.2 Astrophysical probes and the velocity-dependent SIDM

There are many astrophysical probes of SIDM for different halo systems. We summarize the *allowed* values from these probes and the sweet spots for solving small-scale challenges in Fig. 14 as colored bars. The probes are mostly from four classes:

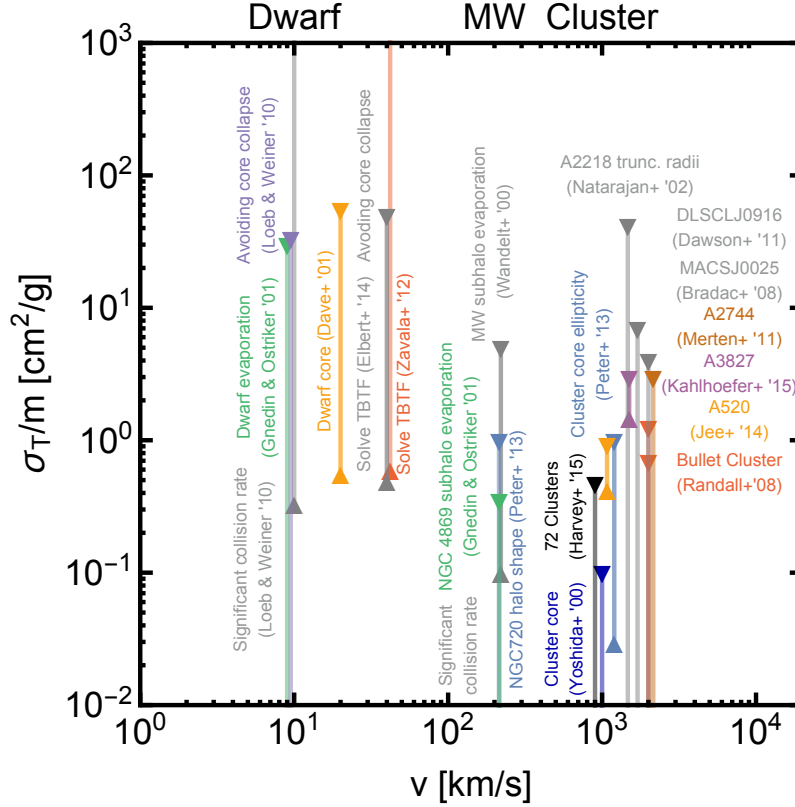


Figure 14. The allowed SIDM cross-section strength as a function of relative velocity of incoming dark matter particles. The probes can be mainly classified into four types: (1) cluster crossing [104–111] (2) core shape [112, 113] (3) core density and density slope [114, 115], and (4) subhalo evaporation [116, 117].

1. Cluster crossing: SIDM leads to smaller separations between the crossed clusters.
2. Core shape: SIDM leads to a more spherical halo core.
3. Core density and density slope: SIDM halos can have a lower density with a flat density slope (core expansion phase) or a higher density with a cuspy density slope (core collapse phase).
4. Subhalo evaporation: SIDM subhalos are more likely to be heated by the host SIDM halo (another type of “core expansion”) and thus evaporate.

See the references in the caption. Ideally, if we can observe the SIDM signatures across all types of probes, this will make a strong case for the SIDM. It is also clear that a velocity-dependent cross-section strength is necessary for SIDM to evade observational constraints and explain the small-scale challenges.

The velocity dependence of SIDM can be effectively realized in the so-called Yukawa SIDM model. This model considers a light scalar with mass m_ϕ mediating the long-range force between dark matter particles with mass m_χ . The self-interaction is described by a Yukawa potential:

	m_χ [GeV]	m_ϕ [MeV]	α_χ
Model 1	119	0.4	3.0×10^{-3}
Model 2	20	3.5	1.6×10^{-3}
Model 3	40	1.1	1.5×10^{-3}
Model 4	18	1.7	1.2×10^{-3}
Model 5	27	1.1	9.0×10^{-4}

Table 3. Benchmarks for the Yukawa SIDM model shown in Fig. 15.

$$V(r) = \pm \alpha_\chi \frac{e^{-m_\phi r}}{r}, \quad (3.44)$$

where α_χ is the strength of the potential, m_ϕ is the mediator mass, and $+$ or $-$ represents a repulsive or attractive interaction, respectively. Given the differential scattering cross-section $d\sigma/d\Omega$ corresponding to $V(r)$, we compute the viscosity transfer cross-section as:

$$\sigma_V = \int \frac{d\sigma}{d\Omega} \sin^2 \theta d\Omega, \quad (3.45)$$

where θ is the scattering angle. The $\sin^2 \theta$ kernel appears from deriving the thermal conductivity [118], which is the key quantity driving the gravothermal evolution of a SIDM halo. The parameter space of the model can be divided into three regimes: the perturbative Born regime ($\alpha_\chi m_\chi / m_\phi \ll 1$), the non-perturbative classical regime ($\alpha_\chi m_\chi / m_\phi \gg 1$, $m_\chi v / m_\phi \gg 1$), and the non-perturbative resonant regime ($\alpha_\chi m_\chi / m_\phi \gg 1$, $m_\chi v / m_\phi \ll 1$). This model exhibits a variety of velocity dependencies, as shown in Fig. 15, which is based on the parameters listed in Tab. 3.2.2. The computational details can be found in [119]. Note that Yukawa SIDM in small halos generally shows a large cross section strength, which could push dwarf halos toward a core-collapsed phase.

Acknowledgments

Y.Z. would like to express gratitude to the organizers, Haipeng An, Lian-Tao Wang, Qing Wang, Yonglong Wang, and Zhong-Zhi Xianyu, for the opportunity to speak and for their efforts in organizing the event. It was a great pleasure to give these lectures, meet students from institutions worldwide, and visit Dai Gu, Linyi, Shangdong, China.

A Units

We often work with natural units, assuming $c = \hbar = k_B = \epsilon_0 = \mu_0 = 1$. In this setup, the elementary charge is $e = \sqrt{4\pi\alpha} = 0.303$. The basic unit conversions between natural units and SI units (kg, m, s, etc.) and astronomical units (M_\odot , pc, year, etc.) can be found at <https://github.com/ymzhong/naturalunit>.

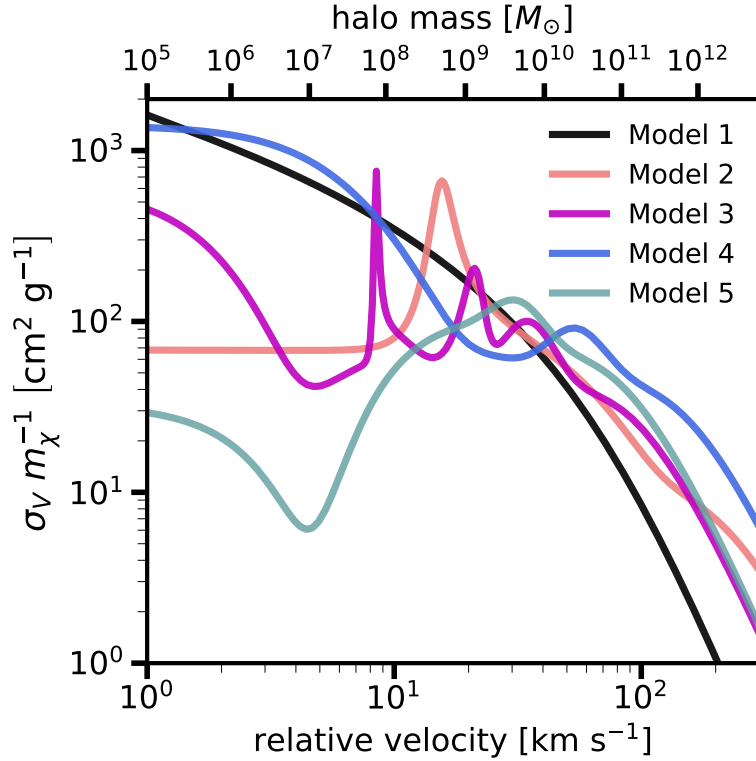


Figure 15. The viscosity transfer cross-section strength σ_V/m_χ for the five benchmark models listed in Tab. 3.2.2, plotted as a function of the relative velocity v (lower x -axis). The upper x -axis shows the halo mass with maximum circular velocity $v_{\text{max}} = v$. The plot is taken from [119].

B Cosmology for students in a hurry

B.1 Background

The evolution of the homogeneous contents of the universe follows the Friedman equation (assuming zero curvature) and the continuity equation. They are respectively given by

$$H^2 = \frac{8\pi G}{3}\rho = H_0^2 (\Omega_{r,0}a^{-4} + \Omega_{m,0}a^{-3} + \Omega_{\Lambda,0}), \quad \dot{\rho} = -3H(\rho + p). \quad (\text{B.1})$$

During different content-dominated eras, the universe expands differently. It evolves from an inflation era to a radiation era, then to a matter era, and finally to a dark energy era. Most of dark matter physics occurs during the radiation and matter eras. The dependence of the energy density ρ , the scale factor a , the Hubble parameter H , and the cosmic time t are summarized in Tab. 4.

From the Planck measurement of Ω_m and COBE’s measurement of the CMB temperature, one can find that matter-radiation equality occurs at $a_{\text{eq}} = 2.9 \times 10^{-4}$, which corresponds to $z_{\text{eq}} = 3400$ or $t_{\text{eq}} \sim 50,000$ years after the Big Bang. This is slightly before recombination at $z_{\text{rec}} = 1270$ or $t_{\text{rec}} \sim 380,000$ years after the Big Bang.

Content	$w \equiv p/\rho$	ρ	a	H
Radiation	1/3	$\frac{3}{32\pi G t^2} \propto a^{-4}$	$\propto t^{1/2}$	$\frac{1}{2t} \propto a^{-2}$
Matter	0	$\frac{1}{6\pi G t^2} \propto a^{-3}$	$\propto t^{2/3}$	$\frac{2}{3t} \propto a^{-\frac{3}{2}}$
Vacuum	-1	$\frac{3H_0^2}{8\pi G}$ (const.)	$e^{H_0 t}$	H_0

Table 4. Different contents of the universe, their equations of state $w \equiv p/\rho$, and the relations between the energy density ρ , scale factor a , Hubble parameter $H \equiv \dot{a}/a$, and time t .

B.2 Thermodynamics in the early universe

Given a distribution function of a system of particles, $f(p, T)$, we can obtain its macroscopic quantities by taking the moment of the distribution function, i.e., integrating over the phase space with some kernel functions. The number density, energy density, and pressure are the moments considered in many Einstein-Boltzmann equations. For a given $f(p, T)$, they are respectively given by

$$n(T) = \frac{g}{(2\pi)^3} \int d^3p f(p, T), \quad (\text{B.2})$$

$$\rho(T) = \frac{g}{(2\pi)^3} \int d^3p f(p, T) E(p), \quad (\text{B.3})$$

$$P(T) = \frac{g}{(2\pi)^3} \int d^3p f(p, T) \frac{p^2}{3E(p)}. \quad (\text{B.4})$$

For bosons and fermions in the early universe, their resulting number density, energy density, and pressure, under the relativistic limit, are respectively given by

$$n = \frac{\zeta(3)}{\pi^2} g T^3 \begin{cases} 1 & \text{boson} \\ \frac{3}{4} & \text{fermion} \end{cases}, \quad \rho = \frac{\pi^2}{30} g T^4 \begin{cases} 1 & \text{boson} \\ \frac{7}{8} & \text{fermion} \end{cases}, \quad P = \frac{\rho}{3} \quad (\text{B.5})$$

If they are non-relativistic, these quantities change to

$$n = g \left(\frac{mT}{2\pi} \right)^{3/2} e^{-m/T}, \quad \rho = mn + \frac{3}{2}nT, \quad P = nT, \quad (\text{B.6})$$

which are all Boltzmann suppressed ($\sim e^{-m/T}$).

If there are multiple relativistic species, the energy density changes to

$$\rho = \frac{\pi^2}{30} g_*(T) T^4 \quad (\text{B.7})$$

where

$$g_* = \sum_{i=b} g_i \left(\frac{T_i}{T} \right)^4 + \frac{7}{8} \sum_{i=f} g_i \left(\frac{T_i}{T} \right)^4 \quad (\text{B.8})$$

The Standard Model at high temperature has 28 degrees of freedom for bosons and 90 degrees of freedom for fermions. Hence the corresponding $g_* = 106.75$.

From the first law of thermodynamics, we have $TdS = dU + PdV$. Now defining the entropy density $s \equiv S/V$ and substituting it together with $U = \rho V$ into the first law gives

$$(Ts - \rho - P)dV + V \left(\frac{Tds}{dT} - \frac{d\rho}{dT} \right) dT = 0 \quad (\text{B.9})$$

For the equation to be always valid, we need

$$s = \frac{\rho + P}{T}, \quad \frac{d(sa^3)}{dt} = 0, \quad (\text{B.10})$$

where the derivation of the second equation uses the continuity equation. The first equation tells us how to compute the specific entropy and the second equation demands the entropy to be conserved.

To compute the specific entropy for multiple relativistic species, from Eq. (B.7), we have

$$s = \frac{2\pi^2}{45} g_{*S}(T) T^3, \quad (\text{B.11})$$

where

$$g_{*S} = \sum_{i=b} g_i \left(\frac{T_i}{T} \right)^3 + \frac{7}{8} \sum_{i=f} g_i \left(\frac{T_i}{T} \right)^3. \quad (\text{B.12})$$

In such a scenario, the entropy conservation, $d(sa^3)/dt$, implies

$$g_{*S}(T) T^3 a^3 = \text{const}, \quad \text{or} \quad T \propto g_{*S}^{-1/3} a^{-1}. \quad (\text{B.13})$$

It will be convenient to define the abundance $Y_i \equiv n_i/s$, which drops out a -dependence if there is no particle creation or annihilation. If dark matter is produced thermally, its abundance Y_i should not change from its freeze-out to today. Given $\rho_{\chi,0} = 10^{-11} \text{ eV}^4 = m_\chi n_{\chi,0}$ and $s_0 \simeq 10^{-11} \text{ eV}^3$, we have

$$Y_\chi \equiv \left(\frac{n_\chi}{s} \right)_0 = \frac{\text{eV}}{m_\chi}. \quad (\text{B.14})$$

B.3 Dark matter thermal freeze-out and the WIMP miracle

The dark matter thermal freeze-out happens when the Hubble parameter catches up with the annihilation rate of dark matter particles into the Standard Model particles.

$$n_\chi \langle \sigma v \rangle \sim H \sim \frac{T_{\text{fo}}^2}{m_{\text{pl}}}, \quad (\text{B.15})$$

where T_{fo} is the freeze-out temperature, which is around $m_\chi/10$. From Eq. (B.15), one can estimate the dark matter abundance Y_χ at freeze-out,

$$(Y_\chi)_{\text{fo}} = \frac{n_{\chi,\text{fo}}}{s_{\text{fo}}} \sim \frac{T_{\text{fo}}^2}{m_{\text{pl}} \langle \sigma v \rangle T_{\text{fo}}^3}. \quad (\text{B.16})$$

From Eq. (B.14), we also have $(Y_\chi)_{\text{fo}} = Y_\chi = \frac{\text{eV}}{m_\chi}$. Combining these two equations and $T_{\text{fo}} \sim m_\chi/10$, we have

$$\langle \sigma v \rangle \sim \frac{10}{\text{eV} m_{\text{pl}}}. \quad (\text{B.17})$$

More careful computation shows that the annihilation cross section needed to obtain the correct dark matter relic abundance is given by

$$\langle\sigma v\rangle = 3 \times 10^{-26} \text{ cm}^2/\text{s} = \frac{1}{(20 \text{ TeV})^2}. \quad (\text{B.18})$$

The cross section seems to indicate dark matter physics should be at the electroweak scales.

References

- [1] M. Cirelli, A. Strumia and J. Zupan, *Dark Matter*, [2406.01705](#).
- [2] S. Dodelson and F. Schmidt, *Modern Cosmology (2nd edition)*. Elsevier Science, 2020.
- [3] D. Baumann, *Cosmology*. Cambridge University Press, 2022.
- [4] T. Lin, *Dark matter models and direct detection*, *PoS* **333** (2019) 009, [[1904.07915](#)].
- [5] B. R. Safdi, *TASI Lectures on the Particle Physics and Astrophysics of Dark Matter*, *PoS TASI2022* (2024) 009, [[2303.02169](#)].
- [6] M. Schmaltz, “Lecture 1 on intro to dark matter.” <https://www.youtube.com/watch?v=WFLSxbcYHp8>, 2020.
- [7] F. Zwicky, *Die Rotverschiebung von extragalaktischen Nebeln*, *Helv. Phys. Acta* **6** (1933) 110–127.
- [8] P. Peebles, *Cosmology’s Century: An Inside History of Our Modern Understanding of the Universe*. Princeton University Press, 2020.
- [9] G. Bertone and D. Hooper, *History of dark matter*, *Rev. Mod. Phys.* **90** (2018) 045002, [[1605.04909](#)].
- [10] PLANCK collaboration, N. Aghanim et al., *Planck 2018 results. VI. Cosmological parameters*, *Astron. Astrophys.* **641** (2020) A6, [[1807.06209](#)].
- [11] N. Bellomo, K. V. Berghaus and K. K. Boddy, *Impact of freeze-in on dark matter isocurvature*, *JCAP* **11** (2023) 024, [[2210.15691](#)].
- [12] A. Strumia, *Dark Matter from freeze-in and its inhomogeneities*, *JHEP* **03** (2023) 042, [[2211.08359](#)].
- [13] D. Racco and A. Riotto, *Freeze-in dark matter perturbations are adiabatic*, *JCAP* **01** (2023) 020, [[2211.08719](#)].
- [14] I. Holst, W. Hu and L. Jenks, *Dark matter isocurvature from curvature*, *Phys. Rev. D* **109** (2024) 063507, [[2311.17164](#)].
- [15] A. Stebbins, *Generation of Isocurvature from Curvature Inhomogeneities on Super-Horizon Scales*, [2311.17379](#).
- [16] Y. Sofue, *Rotation Curve of the Milky Way and the Dark Matter Density*, *Galaxies* **8** (2020) 37, [[2004.11688](#)].
- [17] L. Hui, J. P. Ostriker, S. Tremaine and E. Witten, *Ultralight scalars as cosmological dark matter*, *Phys. Rev. D* **95** (2017) 043541, [[1610.08297](#)].
- [18] J. Alvey, N. Sabti, V. Tiki, D. Blas, K. Bondarenko, A. Boyarsky et al., *New constraints on the mass of fermionic dark matter from dwarf spheroidal galaxies*, *Mon. Not. Roy. Astron. Soc.* **501** (2021) 1188–1201, [[2010.03572](#)].

- [19] J. Lesgourgues and S. Pastor, *Neutrino mass from Cosmology*, [*Adv. High Energy Phys.* **2012** \(2012\) 608515](#), [[1212.6154](#)].
- [20] M. Gerbino et al., *Synergy between cosmological and laboratory searches in neutrino physics*, [*Phys. Dark Univ.* **42** \(2023\) 101333](#), [[2203.07377](#)].
- [21] DESI collaboration, A. G. Adame et al., *DESI 2024 VI: Cosmological Constraints from the Measurements of Baryon Acoustic Oscillations*, [2404.03002](#).
- [22] B. Allanach and H. E. Haber, *Supersymmetry, Part I (Theory)*, [2401.03827](#).
- [23] M. J. Strassler and K. M. Zurek, *Echoes of a hidden valley at hadron colliders*, [*Phys. Lett. B* **651** \(2007\) 374–379](#), [[hep-ph/0604261](#)].
- [24] N. Arkani-Hamed, D. P. Finkbeiner, T. R. Slatyer and N. Weiner, *A Theory of Dark Matter*, [*Phys. Rev. D* **79** \(2009\) 015014](#), [[0810.0713](#)].
- [25] PAMELA collaboration, O. Adriani et al., *An anomalous positron abundance in cosmic rays with energies 1.5–100 GeV*, [*Nature* **458** \(2009\) 607–609](#), [[0810.4995](#)].
- [26] B. Fornal, *Neutron Dark Decay*, [*Universe* **9** \(2023\) 449](#), [[2306.11349](#)].
- [27] Y.-S. Liu, D. McKeen and G. A. Miller, *Electrophobic Scalar Boson and Muonic Puzzles*, [*Phys. Rev. Lett.* **117** \(2016\) 101801](#), [[1605.04612](#)].
- [28] J. L. Feng, B. Fornal, I. Galon, S. Gardner, J. Smolinsky, T. M. P. Tait et al., *Particle physics models for the 17 MeV anomaly in beryllium nuclear decays*, [*Phys. Rev. D* **95** \(2017\) 035017](#), [[1608.03591](#)].
- [29] C.-Y. Chen, J. Kozaczuk and Y.-M. Zhong, *Exploring leptophilic dark matter with NA64- μ* , [*JHEP* **10** \(2018\) 154](#), [[1807.03790](#)].
- [30] PLANCK collaboration, P. A. R. Ade et al., *Planck 2015 results. XIII. Cosmological parameters*, [*Astron. Astrophys.* **594** \(2016\) A13](#), [[1502.01589](#)].
- [31] P. deNiverville, D. McKeen and A. Ritz, *Signatures of sub-GeV dark matter beams at neutrino experiments*, [*Phys. Rev. D* **86** \(2012\) 035022](#), [[1205.3499](#)].
- [32] T. R. Slatyer, *Indirect dark matter signatures in the cosmic dark ages. I. Generalizing the bound on s-wave dark matter annihilation from Planck results*, [*Phys. Rev. D* **93** \(2016\) 023527](#), [[1506.03811](#)].
- [33] M. J. Dolan, T. Ferber, C. Hearty, F. Kahlhoefer and K. Schmidt-Hoberg, *Revised constraints and Belle II sensitivity for visible and invisible axion-like particles*, [*JHEP* **12** \(2017\) 094](#), [[1709.00009](#)].
- [34] Y. Kahn, G. Krnjaic, N. Tran and A. Whitbeck, *M^3 : A New Muon Missing Momentum Experiment to Probe $(g-2)_\mu$ and Dark Matter at Fermilab*, [1804.03144](#).
- [35] A. Berlin, N. Blinov, G. Krnjaic, P. Schuster and N. Toro, *Dark Matter, Millicharges, Axion and Scalar Particles, Gauge Bosons, and Other New Physics with LDMX*, [1807.01730](#).
- [36] M. Battaglieri et al., *US Cosmic Visions: New Ideas in Dark Matter 2017: Community Report*, in *U.S. Cosmic Visions: New Ideas in Dark Matter*, 7, 2017, [1707.04591](#).
- [37] J. Liu, L.-T. Wang, X.-P. Wang and W. Xue, *Exposing the dark sector with future Z factories*, [*Phys. Rev. D* **97** \(2018\) 095044](#), [[1712.07237](#)].
- [38] R. Bollig, H. T. Janka, A. Lohs, G. Martinez-Pinedo, C. J. Horowitz and T. Melson, *Muon*

- Creation in Supernova Matter Facilitates Neutrino-driven Explosions*, *Phys. Rev. Lett.* **119** (2017) 242702, [[1706.04630](#)].
- [39] G. G. Raffelt, *Stars as laboratories for fundamental physics: The astrophysics of neutrinos, axions, and other weakly interacting particles*. 5, 1996.
 - [40] E. Hardy and R. Lasenby, *Stellar cooling bounds on new light particles: plasma mixing effects*, *JHEP* **02** (2017) 033, [[1611.05852](#)].
 - [41] S. Knapen, T. Lin and K. M. Zurek, *Light Dark Matter: Models and Constraints*, *Phys. Rev. D* **96** (2017) 115021, [[1709.07882](#)].
 - [42] B. Batell, A. Freitas, A. Ismail and D. McKeen, *Flavor-specific scalar mediators*, [[1712.10022](#)].
 - [43] J. H. Chang, R. Essig and S. D. McDermott, *Supernova 1987A Constraints on Sub-GeV Dark Sectors, Millicharged Particles, the QCD Axion, and an Axion-like Particle*, *JHEP* **09** (2018) 051, [[1803.00993](#)].
 - [44] M. Pospelov and J. Pradler, *Big Bang Nucleosynthesis as a Probe of New Physics*, *Ann. Rev. Nucl. Part. Sci.* **60** (2010) 539–568, [[1011.1054](#)].
 - [45] S. Navas and P. D. Group, *Review of particle physics*, *Phys. Rev. D* **110** (2024) 030001.
 - [46] T.-H. Yeh, J. Shelton, K. A. Olive and B. D. Fields, *Probing physics beyond the standard model: limits from BBN and the CMB independently and combined*, *JCAP* **10** (2022) 046, [[2207.13133](#)].
 - [47] B. D. Fields and K. A. Olive, *Implications of the non-observation of ${}^6\text{Li}$ in halo stars for the primordial ${}^7\text{Li}$ problem*, *JCAP* **10** (2022) 078, [[2204.03167](#)].
 - [48] K. Akita and M. Yamaguchi, *A precision calculation of relic neutrino decoupling*, *JCAP* **08** (2020) 012, [[2005.07047](#)].
 - [49] Z. Hou, R. Keisler, L. Knox, M. Millea and C. Reichardt, *How Massless Neutrinos Affect the Cosmic Microwave Background Damping Tail*, *Phys. Rev. D* **87** (2013) 083008, [[1104.2333](#)].
 - [50] D. J. Fixsen, *The Temperature of the Cosmic Microwave Background*, *Astrophys. J.* **707** (2009) 916–920, [[0911.1955](#)].
 - [51] K. M. Nollett and G. Steigman, *BBN And The CMB Constrain Light, Electromagnetically Coupled WIMPs*, *Phys. Rev. D* **89** (2014) 083508, [[1312.5725](#)].
 - [52] C. Giovanetti, M. Lisanti, H. Liu and J. T. Ruderman, *Joint Cosmic Microwave Background and Big Bang Nucleosynthesis Constraints on Light Dark Sectors with Dark Radiation*, *Phys. Rev. Lett.* **129** (2022) 021302, [[2109.03246](#)].
 - [53] P. F. Depta, M. Hufnagel and K. Schmidt-Hoberg, *ACROPOLIS: A generiC fRamework fOr Photodisintegration Of LIght elementS*, *JCAP* **03** (2021) 061, [[2011.06518](#)].
 - [54] A. Arbey, J. Auffinger, K. P. Hickerson and E. S. Jenssen, *AlterBBN v2: A public code for calculating Big-Bang nucleosynthesis constraints in alternative cosmologies*, *Comput. Phys. Commun.* **248** (2020) 106982, [[1806.11095](#)].
 - [55] C. Pitrou, A. Coc, J.-P. Uzan and E. Vangioni, *Precision big bang nucleosynthesis with improved helium-4 predictions*, *Submitted to Phys. Rept.* (2018) , [[1801.08023](#)].

- [56] C. Pitrou, A. Coc, J.-P. Uzan and E. Vangioni, *A new tension in the cosmological model from primordial deuterium?*, *Mon. Not. Roy. Astron. Soc.* **502** (2021) 2474–2481, [[2011.11320](#)].
- [57] A.-K. Burns, T. M. P. Tait and M. Valli, *PRyMordial: the first three minutes, within and beyond the standard model*, *Eur. Phys. J. C* **84** (2024) 86, [[2307.07061](#)].
- [58] E. Nadler, *The faintest galaxies and their dark matter halos*, https://cosmology.lbl.gov/talks/Nadler_20.pdf, September, 2020.
- [59] N. Sabti, J. B. Muñoz and D. Blas, *New Roads to the Small-scale Universe: Measurements of the Clustering of Matter with the High-redshift UV Galaxy Luminosity Function*, *Astrophys. J. Lett.* **928** (2022) L20, [[2110.13161](#)].
- [60] S. Chabanier, M. Millea and N. Palanque-Delabrouille, *Matter power spectrum: from Ly α forest to CMB scales*, *Mon. Not. Roy. Astron. Soc.* **489** (2019) 2247–2253, [[1905.08103](#)].
- [61] K. Bechtol et al., *Snowmass2021 Cosmic Frontier White Paper: Dark Matter Physics from Halo Measurements*, in *Snowmass 2021*, 3, 2022, [[2203.07354](#)].
- [62] J. Lesgourgues, *Cosmological Perturbations*, in *Theoretical Advanced Study Institute in Elementary Particle Physics: Searching for New Physics at Small and Large Scales*, 2, 2013, [[1302.4640](#)], DOI.
- [63] E. W. Kolb, *The Early Universe*, vol. 69. Taylor and Francis, 5, 2019, [[10.1201/9780429492860](#)].
- [64] P. Bode, J. P. Ostriker and N. Turok, *Halo formation in warm dark matter models*, *Astrophys. J.* **556** (2001) 93–107, [[astro-ph/0010389](#)].
- [65] A. Schneider, R. E. Smith, A. V. Maccio and B. Moore, *Nonlinear Evolution of Cosmological Structures in Warm Dark Matter Models*, *Mon. Not. Roy. Astron. Soc.* **424** (2012) 684, [[1112.0330](#)].
- [66] R. Feynman, R. Leighton and M. Sands, *The Feynman Lectures on Physics*. No. Vol. 1~3 in Addison-Wesley world student series. Addison-Wesley Publishing Company, 1963.
- [67] K. K. Rogers and H. V. Peiris, *Strong Bound on Canonical Ultralight Axion Dark Matter from the Lyman-Alpha Forest*, *Phys. Rev. Lett.* **126** (2021) 071302, [[2007.12705](#)].
- [68] M. A. Buen-Abad, R. Essig, D. McKeen and Y.-M. Zhong, *Cosmological constraints on dark matter interactions with ordinary matter*, *Phys. Rept.* **961** (2022) 1–35, [[2107.12377](#)].
- [69] E. O. Nadler, V. Gluscevic, K. K. Boddy and R. H. Wechsler, *Constraints on Dark Matter Microphysics from the Milky Way Satellite Population*, *Astrophys. J. Lett.* **878** (2019) 32, [[1904.10000](#)].
- [70] DES collaboration, E. O. Nadler et al., *Milky Way Satellite Census. III. Constraints on Dark Matter Properties from Observations of Milky Way Satellite Galaxies*, *Phys. Rev. Lett.* **126** (2021) 091101, [[2008.00022](#)].
- [71] O. Newton, M. Leo, M. Cautun, A. Jenkins, C. S. Frenk, M. R. Lovell et al., *Constraints on the properties of warm dark matter using the satellite galaxies of the Milky Way*, [[2011.08865](#)].
- [72] N. Banik, J. Bovy, G. Bertone, D. Erkal and T. J. L. de Boer, *Novel constraints on the particle nature of dark matter from stellar streams*, [[1911.02663](#)].

- [73] E. O. Nadler, S. Birrer, D. Gilman, R. H. Wechsler, X. Du, A. Benson et al., *Dark Matter Constraints from a Unified Analysis of Strong Gravitational Lenses and Milky Way Satellite Galaxies*, [2101.07810](#).
- [74] W. Enzi et al., *Joint constraints on thermal relic dark matter from a selection of astrophysical probes*, [2010.13802](#).
- [75] D. McCammon et al., *A High spectral resolution observation of the soft x-ray diffuse background with thermal detectors*, *Astrophys. J.* **576** (2002) 188–203, [[astro-ph/0205012](#)].
- [76] A. L. Erickcek, P. J. Steinhardt, D. McCammon and P. C. McGuire, *Constraints on the Interactions between Dark Matter and Baryons from the X-ray Quantum Calorimetry Experiment*, *Phys. Rev. D* **76** (2007) 042007, [[0704.0794](#)].
- [77] M. S. Mahdawi and G. R. Farrar, *Constraints on Dark Matter with a moderately large and velocity-dependent DM-nucleon cross-section*, *JCAP* **10** (2018) 007, [[1804.03073](#)].
- [78] CRESST collaboration, A. H. Abdelhameed et al., *First results from the CRESST-III low-mass dark matter program*, *Phys. Rev. D* **100** (2019) 102002, [[1904.00498](#)].
- [79] CRESST collaboration, A. H. Abdelhameed et al., *Description of CRESST-III Data*, [1905.07335](#).
- [80] CRESST collaboration, G. Angloher et al., *Results on MeV-scale dark matter from a gram-scale cryogenic calorimeter operated above ground*, *Eur. Phys. J. C* **77** (2017) 637, [[1707.06749](#)].
- [81] XENON collaboration, E. Aprile et al., *First Dark Matter Search Results from the XENON1T Experiment*, *Phys. Rev. Lett.* **119** (2017) 181301, [[1705.06655](#)].
- [82] EDELWEISS collaboration, E. Armengaud et al., *Searching for low-mass dark matter particles with a massive Ge bolometer operated above-ground*, *Phys. Rev. D* **99** (2019) 082003, [[1901.03588](#)].
- [83] W. Yin, *Highly-boosted dark matter and cutoff for cosmic-ray neutrinos through neutrino portal*, *EPJ Web Conf.* **208** (2019) 04003, [[1809.08610](#)].
- [84] T. Bringmann and M. Pospelov, *Novel direct detection constraints on light dark matter*, *Phys. Rev. Lett.* **122** (2019) 171801, [[1810.10543](#)].
- [85] C. Cappiello and J. F. Beacom, *Strong New Limits on Light Dark Matter from Neutrino Experiments*, *Phys. Rev. D* **100** (2019) 103011, [[1906.11283](#)].
- [86] D. Wadekar and G. R. Farrar, *First astrophysical constraints on dark matter interactions with ordinary matter at low relative velocity*, [1903.12190](#).
- [87] T. Emken, R. Essig, C. Kouvaris and M. Sholapurkar, *Direct Detection of Strongly Interacting Sub-GeV Dark Matter via Electron Recoils*, *JCAP* **09** (2019) 070, [[1905.06348](#)].
- [88] R. Essig, A. Manalaysay, J. Mardon, P. Sorensen and T. Volansky, *First Direct Detection Limits on sub-GeV Dark Matter from XENON10*, *Phys. Rev. Lett.* **109** (2012) 021301, [[1206.2644](#)].
- [89] R. Essig, T. Volansky and T.-T. Yu, *New Constraints and Prospects for sub-GeV Dark Matter Scattering off Electrons in Xenon*, *Phys. Rev. D* **96** (2017) 043017, [[1703.00910](#)].
- [90] XENON10 collaboration, J. Angle et al., *A search for light dark matter in XENON10 data*, *Phys. Rev. Lett.* **107** (2011) 051301, [[1104.3088](#)].

- [91] XENON collaboration, E. Aprile et al., *Low-mass dark matter search using ionization signals in XENON100*, *Phys. Rev. D* **94** (2016) 092001, [[1605.06262](#)].
- [92] DARKSIDE collaboration, P. Agnes et al., *Constraints on Sub-GeV Dark-Matter–Electron Scattering from the DarkSide-50 Experiment*, *Phys. Rev. Lett.* **121** (2018) 111303, [[1802.06998](#)].
- [93] SUPERCDMS collaboration, R. Agnese et al., *First Dark Matter Constraints from a SuperCDMS Single-Charge Sensitive Detector*, *Phys. Rev. Lett.* **121** (2018) 051301, [[1804.10697](#)].
- [94] SENSEI collaboration, M. Crisler, R. Essig, J. Estrada, G. Fernandez, J. Tiffenberg, M. Sofo haro et al., *SENSEI: First Direct-Detection Constraints on sub-GeV Dark Matter from a Surface Run*, *Phys. Rev. Lett.* **121** (2018) 061803, [[1804.00088](#)].
- [95] SENSEI collaboration, O. Abramoff et al., *SENSEI: Direct-Detection Constraints on Sub-GeV Dark Matter from a Shallow Underground Run Using a Prototype Skipper-CCD*, *Phys. Rev. Lett.* **122** (2019) 161801, [[1901.10478](#)].
- [96] SENSEI collaboration, L. Barak et al., *SENSEI: Direct-Detection Results on sub-GeV Dark Matter from a New Skipper-CCD*, *Phys. Rev. Lett.* **125** (2020) 171802, [[2004.11378](#)].
- [97] Y. Ema, F. Sala and R. Sato, *Light Dark Matter at Neutrino Experiments*, *Phys. Rev. Lett.* **122** (2019) 181802, [[1811.00520](#)].
- [98] H. An, M. Pospelov, J. Pradler and A. Ritz, *Directly Detecting MeV-scale Dark Matter via Solar Reflection*, *Phys. Rev. Lett.* **120** (2018) 141801, [[1708.03642](#)].
- [99] T. Emken, *Solar reflection of light dark matter with heavy mediators*, [2102.12483](#).
- [100] D. J. Fixsen, E. S. Cheng, J. M. Gales, J. C. Mather, R. A. Shafer and E. L. Wright, *The Cosmic Microwave Background spectrum from the full COBE FIRAS data set*, *Astrophys. J.* **473** (1996) 576, [[astro-ph/9605054](#)].
- [101] Y. Ali-Haïmoud, J. Chluba and M. Kamionkowski, *Constraints on Dark Matter Interactions with Standard Model Particles from Cosmic Microwave Background Spectral Distortions*, *Phys. Rev. Lett.* **115** (2015) 071304, [[1506.04745](#)].
- [102] Y. Ali-Haïmoud, *Testing dark matter interactions with CMB spectral distortions*, *Phys. Rev. D* **103** (2021) 043541, [[2101.04070](#)].
- [103] S. Tulin and H.-B. Yu, *Dark Matter Self-interactions and Small Scale Structure*, *Phys. Rept.* **730** (2018) 1–57, [[1705.02358](#)].
- [104] S. W. Randall, M. Markevitch, D. Clowe, A. H. Gonzalez and M. Bradac, *Constraints on the Self-Interaction Cross-Section of Dark Matter from Numerical Simulations of the Merging Galaxy Cluster 1E 0657-56*, *Astrophys. J.* **679** (2008) 1173–1180, [[0704.0261](#)].
- [105] D. Harvey, R. Massey, T. Kitching, A. Taylor and E. Tittley, *The non-gravitational interactions of dark matter in colliding galaxy clusters*, *Science* **347** (2015) 1462–1465, [[1503.07675](#)].
- [106] M. J. Jee, H. Hoekstra, A. Mahdavi and A. Babul, *Hubble Space Telescope/Advanced Camera for Surveys Confirmation of the Dark Substructure in A520*, *Astrophys. J.* **783** (2014) 78, [[1401.3356](#)].
- [107] P. Natarajan, A. Loeb, J.-P. Kneib and I. Smail, *Constraints on the collisional nature of the*

- dark matter from gravitational lensing in the cluster a2218, *Astrophys. J. Lett.* **580** (2002) L17–L20, [[astro-ph/0207045](#)].
- [108] W. A. Dawson et al., *Discovery of a Dissociative Galaxy Cluster Merger with Large Physical Separation*, *Astrophys. J. Lett.* **747** (2012) L42, [[1110.4391](#)].
 - [109] M. Bradac, S. W. Allen, T. Treu, H. Ebeling, R. Massey, R. G. Morris et al., *Revealing the properties of dark matter in the merging cluster MACSJ0025.4-1222*, *Astrophys. J.* **687** (2008) 959, [[0806.2320](#)].
 - [110] J. Merten et al., *Creation of cosmic structure in the complex galaxy cluster merger Abell 2744*, *Mon. Not. Roy. Astron. Soc.* **417** (2011) 333–347, [[1103.2772](#)].
 - [111] F. Kahlhoefer, K. Schmidt-Hoberg, J. Kummer and S. Sarkar, *On the interpretation of dark matter self-interactions in Abell 3827*, *Mon. Not. Roy. Astron. Soc.* **452** (2015) L54–L58, [[1504.06576](#)].
 - [112] A. H. G. Peter, M. Rocha, J. S. Bullock and M. Kaplinghat, *Cosmological Simulations with Self-Interacting Dark Matter II: Halo Shapes vs. Observations*, *Mon. Not. Roy. Astron. Soc.* **430** (2013) 105, [[1208.3026](#)].
 - [113] N. Yoshida, V. Springel, S. D. M. White and G. Tormen, *Collisional dark matter and the structure of dark halos*, *Astrophys. J. Lett.* **535** (2000) L103, [[astro-ph/0002362](#)].
 - [114] R. Dave, D. N. Spergel, P. J. Steinhardt and B. D. Wandelt, *Halo properties in cosmological simulations of selfinteracting cold dark matter*, *Astrophys. J.* **547** (2001) 574–589, [[astro-ph/0006218](#)].
 - [115] A. Loeb and N. Weiner, *Cores in Dwarf Galaxies from Dark Matter with a Yukawa Potential*, *Phys. Rev. Lett.* **106** (2011) 171302, [[1011.6374](#)].
 - [116] O. Y. Gnedin and J. P. Ostriker, *Limits on collisional dark matter from elliptical galaxies in clusters*, *Astrophys. J.* **561** (2001) 61, [[astro-ph/0010436](#)].
 - [117] B. D. Wandelt, R. Dave, G. R. Farrar, P. C. McGuire, D. N. Spergel and P. J. Steinhardt, *Selfinteracting dark matter*, in *4th International Symposium on Sources and Detection of Dark Matter in the Universe (DM 2000)*, pp. 263–274, 6, 2000, [astro-ph/0006344](#).
 - [118] E. M. Lifshitz and L. P. Pitaevskii, *Physical kinetics*. 1981.
 - [119] D. Gilman, Y.-M. Zhong and J. Bovy, *Constraining resonant dark matter self-interactions with strong gravitational lenses*, *Phys. Rev. D* **107** (2023) 103008, [[2207.13111](#)].